A novel supercritical CO_2 recompression Brayton power cycle for power tower concentrating solar plants

José I. Linares[a],[*], María J. Montes[b], Alexis Cantizano[a], Consuelo Sánchez[b]

[a] Comillas Pontifical University, Alberto Aguilera, 25, 28015 Madrid, Spain
[b] Universidad Nacional de Educación a Distancia (UNED), Juan del Rosal 12, 28040 Madrid, Spain

HIGHLIGHTS

- Feasibility of high temperature molten salts concentrated solar plants is assessed.
- A novel S-CO_2 Brayton power cycle with low pressure side heat supply is proposed.
- Novel cycle allows to avoid clogging issues using shell and tube heat exchangers.
- A cavity receiver is proposed to work at high temperature to minimize radiation loss.
- Estimated investment is in accordance with Solar Power Gen3 Demonstration Roadmap.

ARTICLE INFO

ABSTRACT

Power tower concentrating solar plants with thermal energy storage will play a key role in the transition to a low carbon scenario, thanks to be a dispatchable renewable energy system. The ternary $MgCl_2$/KCl/NaCl salt appears as one of the most promising due to its lower melting point, higher heat capacity, lower cost and stability up to 800 °C. A cavity-type receiver has been selected because minimizes radiation heat loss at high working temperatures, compared to an external-type receiver, since all commercial selective coatings degrade in air. Supercritical Brayton power cycle is chosen for the power block because it can surpass 50% efficiency, even when working in dry cooling conditions, and printed circuit heat exchangers are usually recommended due to its ability to support the high pressures. However, plugging/clogging issues arise in their small channels when using molten salts. This paper proposes a novel supercritical CO_2 Bayton power cycle whose heat power is supplied through the low pressure side (over 85 bar) allowing the use of shell and tube heat exchangers, achieving a higher compactness and a lower investment. Thus, different options based on the recompression layout with intercooling and reheating have been investigated in both dry and wet cooling scenarios. Reheating is recommended for wet cooling, reaching 54.6% efficiency and an investment of 8662 \$/kWe; intercooling with reheating is the best option for dry cooling, reaching 52.6% efficiency and an investment of 8742 \$/kWe.

1. Introduction

The progressive replacement of fossil power plants by clean energy technologies is one of the challenges facing humanity today. Among clean energies, the renewable ones have an important role, especially due to their local origin. However, the most currently developed renewable energies (solar PV and wind) have the limitation of intermittency, which leads to fossil back-up systems. This issue is tackled by using energy storage systems in the power plants, being the solar thermal energy storage (TES), used in the concentrated solar power (CSP) plants, one of the most promising technologies. These plants face

to several challenges, including the currently high generation costs, but the advantages of the TES makes them a promising alternative in a future energy scenario that avoids global warming. In this way, the Solar Power Gen3 Demonstration Roadmap from the National Renewable Energies Laboratory (NREL) [1] has focused on power tower solar (PTS) systems with three pathways to TES: molten salts, falling particle and gas phase, establishing some cost goals. For all the alternative pathways, the Roadmap proposes the supercritical CO_2 Brayton power cycle (S-CO_2). NREL proposed a demonstration facility of 10 MWe with a cost over \$200 million, although with a notable uncertainty. The receiver should work at high temperature (above

---

* Corresponding author.
  E-mail address: linares@comillas.edu (J.I. Linares).

Nomenclature

Acronyms

AC	Auxiliary Compressor
ASME	American Society of Mechanical Engineers
CP	Cooling pump
CSP	Concentrating Solar Plants
FCI	Fixed Capital Investment
HPT	High Pressure Turbine
HTF	Heat Transfer Fluid
HTP	High Temperature Pump (in the heating loop)
HTR	High Temperature Recuperator
IC	Intercooling, intercooler
LP	Low Pressure heat power feeding
LPT	Low Pressure Turbine
LTP	Low Temperature Pump (in the heating loop)
LTR	Low Temperature Recuperator
MC	Main Compressor
MC1	Low Pressure Main Compressor
MC2	High Pressure Main Compressor
MCIT	Main Compressor Inlet Temperature
MS	Molten Salt
NREL	National Renewable Energies Laboratory
OFFSC	Off-site Costs
ONSC	On-site Costs
p	Pressure
PC	Pre-cooler
PCHE	Printed Circuit Heat Exchanger
PEC	Purchased-Equipment Costs
PTS	Power Tower Solar
RC	S-CO_2 Recompression layout
RH	Reheating, reheater
S-CO_2	Supercritical Brayton Power Cycle
SHX	Source Heat Exchanger
SHXIT	CO_2 inlet temperature to the Source Heat Exchanger
SNL	Sandia National Laboratory
STHE	Shell and Tubes Heat Exchanger
T	Temperature, Turbine
TEMA	Tubular Exchanger Manufacturers Association
TES	Thermal Energy Storage
TIP	Turbine Inlet Pressure

Latin letters

A	Surface
a	Escalation factor
c	Specific heat; Mean velocity
C	Cost
CI	Cost index
D	Diameter
F	View factor
f	Factor; Darcy friction factor
G	Solar flux
h	Height; Enthalpy; convection heat transfer coefficient
I	Radiosity
L	Flow path length
M	Generic Magnitude
$\dot{m}$	Mass flow rate
Nu	Nusselt number
P	Pressure
P	Wetted perimeter
$\dot{Q}$	Heat transfer
$\dot{q}$	Heat transfer flux
Ra	Rayleigh number
s	Entropy
T	Temperature
U	Overall heat transfer coefficient
$\dot{W}$	Power
Z_w	Angle between the z-axis and the normal vector to the surface

Greek Letters

α	Ratio of cold to hot mass flow rate streams at LTR
Δ	Decrement
δ_{ij}	Kronecker delta
ε	Emissivity
η	Cycle/receiver efficiency; Isentropic efficiency
ρ	Density
σ	Stefan-Boltzmann constant

Subscripts

0	Base case
0y	Base reference year
A	Heat transfer area
AC	Auxiliary Compressor
amb	Ambient
b	Baseline heat exchanger cost
c	Compressor; Cold
conv	convection
CP	Cooling pump
cycle	Cycle
E	Cost referred to 1982
ERy	Cost corrected to the reference year "y"
f	Cost multiplier in shell and tube cost estimation
g	Generator
gross	Gross
h	Hot
HPT	High Pressure Turbine
HTP	High Temperature Pump (in the heating loop)
i	Correcting factors in shell and tube cost estimation; Inlet; i-th element
j	j-th element
LPT	Low Pressure Turbine
LTP	Low Temperature Pump (in the heating loop)
loss	Heat loss
MC	Main Compressor
MC1	Low Pressure Main Compressor
MC2	High Pressure Main Compressor
mix	Mixture
net	Net
o	Outlet
p	Pressure; Cost multiplier in shell and tube cost estimation
r	Cost multiplier in shell and tube cost estimation
Ry	Reference year "y"
rad	Radiation
s	Solar (super-index)
sh	Shell
T	Turbine; Temperature
t	Tower
th	Thermal
TMG	Turbomachines and Generator
tower	Tower
W	Power

700 °C), which leads to replace the typical solar salt by another that is capable to maintain stability at such temperatures. Regarding the power cycle, the main goal is to reach efficiencies higher than 50%. Similar goals are proposed in other research programmes, as in the Australian Solar Thermal Research Initiative (ASTRI) [2] or in the project developed by EDF in collaboration with Zhejiang University, to design a 100 MWe plant with S-CO$_2$, and molten salt (MS) as TES with power tower technology [3].

As conventional solar salts (nitrate salts) cannot be used above 600 °C, it is necessary to replace them in order to meet the target temperature of 700 °C or even higher values. Myers and Goswami [4] show a review of chloride salts and their eutectics, which might be used for sensible or even latent TES. Li et al. [5] give equations for thermophysical properties of both binary and ternary eutectic salts from NaCl, KCl, MgCl$_2$, CaCl$_2$ and ZnCl$_2$, which are able to be used up to 800 °C. They recommend these salts as heat transfer fluids (HTF) in CSP. Mohan et al. [6] assess the thermophysical properties and cost of a novel ternary eutectic salt mixture composed of NaCl, KCl and MgCl$_2$ for high temperature sensible storage. This novel salt mixture has a melting point of 387 °C and is stable up to 800 °C, which makes it suitable for advanced power tower technology with two tank storage based in 500/700 °C. Besides that, this salt has a 32% lower volumetric heat capacity (ρc), compared to conventional salts, requiring a smaller volume of the storage tanks, given that tank size is inversely proportional to $\rho c_p \cdot \Delta T$. At last, its cost (currency 2016) is 295 \$/tonne, which makes it competitive with nitrate salts (over 1000 \$/tonne, [1]). According to these authors, this novel ternary salt is the most promising candidate for high temperature applications. Xu et al. [7] show experimental data for the properties of this novel salt.

The receiver configuration selected is a tubular cavity-type. Although the current state-of-art configuration for MS receivers is the tubular external-type [1], recent research [8] recommends the cavity design as a way not to penalize thermal efficiency when working at high temperature, and radiation heat loss becomes important. Cavity receivers are generally expected to have a lower radiation heat loss than external receivers, although a selective coating for tubes that withstand high temperature and does not degrade in air is not commercially available yet. A north-facing heliostat field is associated to these cavity-receivers. For all the layouts analysed in this work, the solar multiple is equal to 1.5; this value is a compromise between the energy availability in the thermal storage and acceptable receiver dimensions, as cavity receivers require a larger absorber surface area than external receivers [9].

The conventional Brayton cycle (using an ideal gas as working fluid) presents the advantage of a high compactness due to the small size of the turbomachinery and also to a simpler layout than the steam Rankine cycle. However, it demands a high compression power, an issue which is overcome with high turbine inlet temperatures, usually around 1200 °C and higher [10]. To maintain high efficiency at lower temperatures the working fluid should be replaced. So, using Helium in a closed cycle, efficiencies higher than 50% can be reached in high temperature reactors foreseen in nuclear fission Generation IV [11]. However, helium demands temperatures around 850–950 °C to reach high efficiencies. When temperature approximates 500 °C, as in sodium fast reactors (another design foreseen in Generation IV), Brayton cycles with helium reduce considerably their efficiency [12]. It is in these cases when the use of supercritical CO$_2$ as working fluid allows reaching again high efficiencies [13].

The first proposals of CO$_2$ Brayton power cycles come from Sulzer in 1950 [14]. Nearly twenty years later, Angelino [15] analysed several layouts of transcritical cycles, that is, with the heat rejection pressure below the critical pressure, which leads to condensation during the heat rejection process. This application requires a low heat sink temperature due to the low critical temperature of the CO$_2$ (around 31 °C). At the same time, Feher [16] proposed the so-called supercritical cycle, that is, all the cycle working above the supercritical pressure. However, likely

due to the lack of technology for the required turbomachines, the researchers did not pay attention to S-CO$_2$ until 2004, when Dostal [17] retook the cycle as the power conversion system for sodium fast reactors (nuclear fission Generation IV programme). The key aspect of the S-CO$_2$ is the closeness of the compressor inlet conditions to the critical point. In such region (above the critical pressure, but not far, usually between 75 and 90 bar) the density of CO$_2$ is high, thus reducing the compression power very much and allowing the use of moderate turbine inlet temperatures. So, 500 °C is enough to reach an efficiency of 40%, achieving higher values than with supercritical steam Rankine cycle, for turbine inlet temperatures higher than 550 °C [17].

When moderate to high temperatures in the thermal source are available, the S-CO$_2$ employs recuperators, that is, heat exchangers that recover the thermal energy in the fluid, which leaves the turbine, to pre-heat the fluid before it enters the heat source. The closeness of part of the cycle to the critical point makes the heat recovery process complex, which is overcome with different arrangements, being the so called recompression the most common [17]. On the one hand, depending on the source and heat sink temperatures, variations including intercooling and reheating are possible. So, Wang et al. [18] conclude that intercooling increases the efficiency at high compressor inlet temperatures (when dry cooling is used) and that reheating should be always included in S-CO$_2$ for CSP applications, although it tends to reduce the molten salt temperature difference, so increasing the salt inventory. Ma et al. [19] also recommend intercooling when dry cooling is used. Similar results are obtained by Binotti et al. [20]. On the other hand, Pérez-Pichel [13] does not recommend neither intercooling nor reheating for sodium fast reactor applications (turbine inlet temperature about 500 °C).

Regarding the use of S-CO$_2$ in CSP, especially in the power tower solar plants, the research is recent. So, Iverson and Conboy in 2013 [21] claimed that the publications and research works for nuclear applications (focused on Generation IV) have experienced a large development, including experimental work, whereas the analysis for CSP is lower, in comparison. Later, some authors have paid attention to other applications, as it can be seen in the review carried out by Ahn et al. [22]. Li et al. [23] reviewed nuclear, solar energy, geothermal, waste heat recovery and fuel cell, gathering a survey about experimental facilities around the world. Turchi et al. [24] focused on CSP, covering the dry cooling, intercooling and reheating. Milani et al. [25] proposed a hybrid fossil/solar design based on recompression with intercooling and reheating as a contribution to the transition to a low-carbon industry. Most recently, Wang et al. [26] developed a multi-objective optimisation to select the best layout, finding the recompression with intercooling if high compressor inlet temperature is reached (dry cooling scenarios).

The high compactness of S-CO$_2$ power cycles has revealed as one of its most attractive features. So, Xu et al. [27] highlight the good dynamic response of the heat exchangers and the small turbomachines, which lead to supply grid stability against dynamic changes. This good behaviour against fluctuations was also observed by Iverson et al. [21] with small scale experiments, and predicted by Ma et al. [28], who analysed a PTS in direct cycle.

Dostal [17] recommends printed circuit heat exchangers (PCHE) for S-CO$_2$ power cycles. This type of heat exchangers usually uses small semi-circular channels (around 2 mm diameter) in a very compact arrangement, achieving temperature approaches of 2 °C, which leads to effectiveness as high as 98%. They are manufactured with diffusion bonding technology, which allows them to support high pressures (up to 800 bar) [29]. They can be manufactured in SS 316, recommended for temperatures up to 500 °C, and in Inconel 617 for higher [30]. Huang et al. [31] gathered several correlations to describe the flow and heat transfer mechanisms in PCHEs.

From the point of view of the integration of the CSP into the grid, the most important issue is the ability to store energy, so improving the dispatchability [1]. However, several authors have warned about

certain aspects of the use of molten salts in PCHEs. So, Moore et al. [32] discuss different types of heat exchangers for PTS with molten salts, stating that PCHEs technology is unproven in many applications, expressing doubts about maintenance and cleaning, and highlighting that plugging caused by salts can be a serious problem. In similar way, Sabharwall et al. [33] point out the thawing/clogging as a criterion to select the type of heat exchanger to be used with molten salts, indicating that PCHEs currently exhibits some concerns. In order to overcome them, some authors have studied a modified PCHE with airfoils fins in the salt side and with the common channels in the CO_2 side. So, Lao et al. [34] have analysed such solutions, concluding that a deterioration in the heat transfer mechanism is observed. Wang et al. [35] carried out an experimental work using the airfoil fins. They established that shell and tubes heat exchangers (STHE) are not suitable for pressures higher than 200 bar, values usually found at S-CO_2. Another modification of PCHEs to avoid the salt issues is the replacement of the usual channels in the salt side by a rectangular fin structure (hybrid heat exchanger), resulting in a larger cross-section for the salt. Unfortunately, this solution is only valid again up to 200 bar, thus introducing limitations in the performance of the S-CO_2 cycle [36]. In spite of the pressure restrictions of the STHE, some authors advocate their use, as He et al. [37], who carry out experimental investigations, or Qiu et al. [38] who propose a new design of STHE, although they perform the analysis with molten salt in the shell and oil in the tubes side. Finally, Zhang et al. [3] propose STHE for the molten salt/CO_2 heat exchanger in a PTS with S-CO_2 and PCHEs for the recuperators, but with a maximum pressure of the cycle of 200 bar.

One way forward to use STHE in S-CO_2, with pressures higher than 200 bar, would be to supply the heat power to the cycle at a pressure lower than the maximum. This can be done in the so-called split expansion cycle, where the heat power is supplied at an intermediate pressure between two turbines, as in a reheating, and the heat transfer upstream the high pressure turbine comes from the recuperator, fed with the flow leaving the low pressure turbine [18].

As indicated in the references mentioned above, advanced concentrated solar plants based on S-CO_2 power cycles must address three main challenges: first, the stability of the molten salt at high working temperature; second, the requirement of an efficiency higher than 50% for the S-CO_2 power cycle to be economically viable; and third, the thawing/clogging issues of the molten salt through the narrow channels of the salt/CO_2 heat exchanger. The first challenge seems to be overcome by using a new generation of molten salts, such as the ternary chloride molten salt used in this work. However, the high power cycle efficiency, required in the second challenge, yields to a high pressure at the turbine inlet, as well as to the need for reheating (and eventually intercooling in case of a dry cooling scenario). These restrictions also lead to large pressure differences between the streams in the source heat exchangers, which are usually designed as PCHE to withstand such mechanical loads. Unfortunately, the required use of PCHE involves potential clogging issues of the molten salt, which is the last challenge.

Nevertheless, the technical feasibility of these advanced concentrated solar plants based on S-CO_2 is achieved with the novel cycle presented in this study. This novel cycle is able to address the three challenges described above, in particular, the last one, by supplying the source heat on the low pressure side; in this way, the source heat exchangers are designed as conventional shell and tubes heat exchangers, with the molten salt flowing through the shell and thus avoiding the clogging issues. This novel cycle has been designed and simulated, assessing the efficiency at nominal conditions, for both dry and wet cooling scenarios; the shell and tubes source heat exchangers have been designed and calculated according with Tubular Exchanger Manufacturers Association (TEMA) standards. The central receiver has been designed as a cavity-type, as is recommended in recent studies [8], in order to reduce the radiation heat loss when working at high temperature, compared to conventional external receiver designs with molten salts. The heliostat field has been oversized with a solar multiple

of 1.5, as a compromise between the plant dispatchability and the receiver dimensions, which are larger for cavity-type compared to external designs for the same power. Investment assessment has been also carried out in order to verify the compliance with Gen3 forecasts [1].

Solar Power Gen3 faces to additional challenges that are analysed in the Demonstration Roadmap from NREL [1]. These mainly concern materials that can achieve acceptable strength, durability and cost targets at high temperatures. Corrosion mechanism of selected salts should be provided to component designers. Once salt and containment materials are selected, design challenges are expected to be similar to the ones in Solar Two project, although a redesign of some components, as the hot tank, might be necessary. From the point of view of reliability, experience in current CSP plants shows that construction and quality control are key factors. The roadmap points out that the operation at high temperatures requires systems as simple as possible, which opens room to S-CO_2 power block, with a simpler arrangement than in a classical Rankine power plant. In addition, molten-salt technology is the most familiar of the three paths proposed by Gen3. NREL is working with the industry and stakeholders since August 2016 to go ahead with the roadmap towards the commercialization.

2. Methodology

2.1. Cycle layouts

As it has been mentioned in the previous section, the use of molten salts is discouraged in PCHEs due to the narrow channels (2 mm diameter). So, Moore et al. [32] point out concerns about inspections and maintenance, indicating that there are not known cleaning methods. Similarly, Sabharwall et al. [33] propose a parallel research of PCHEs and helical coil heat exchangers for nuclear power plants cooled with molten salts, recommending the use of helical coil heat exchangers as first-of-a-kind option. Wang et al. [35] revise alternative PCHE designs to be used with molten salts, replacing the narrow channels by some type of fins, and obtaining experimental results with airfoil fins. Iverson et al. [21] indicate that the channel dimensions used for CO_2 are not suitable for salts due to the concern for plugging of solidified salts. So, a hybrid heat exchanger is required, with wider channels for the salt stream. However, a larger flow-passage section for the salt stream leads to a reduction in the withstanding operation pressure, especially over 600 °C [29]. Thus, the limit of 200 bar established for shell and tube heat exchangers [35] is reached again.

The main key of the novel energy conversion system proposed is the heat power supply through the low pressure side. This enables the possibility of replacing the printed circuit heat exchanger by a more mature shell and tubes heat exchanger, with the molten salt flowing inside the shell, so avoiding the thawing/clogging issues. As the shell and tube heat exchanger will operate at a pressure lower than 200 bar, its investment is expected to be lower than in a conventional S-CO_2 power cycle where the shell and tube heat exchanger is located upstream the turbine inlet and is operating at 200 bar to maintain high efficiency [3].

Fig. 1 shows a comparison between the conventional recompression cycle (RC) and the novel cycle fed at low pressure (RC-LP). It is observed that in the novel design the heat power is transferred to the upstream turbine flow by means of the high temperature recuperator (HTR). Both cycles are based on the recompression concept, that is, the use of two compressors (main compressor, MC, and auxiliary compressor, AC) to manage the main issue of the supercritical CO_2 closeness to the critical point, that is, the clearly different value of specific heat with the pressure. So, the high pressure stream leaving the main compressor (6 in Fig. 1a and 7 in Fig. 1b) exhibits a higher specific heat than the low pressure stream coming to the low temperature recuperator (LTR) (3 in Fig. 1a and 4 in Fig. 1b). These different values of the specific heat lead to locate the minimum temperature approach in the cold stream inlet, with a large temperature approach in the cold stream
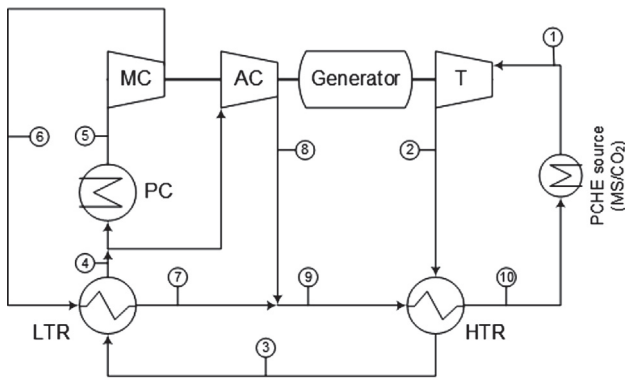
(a) Conventional recompression cycle (RC)
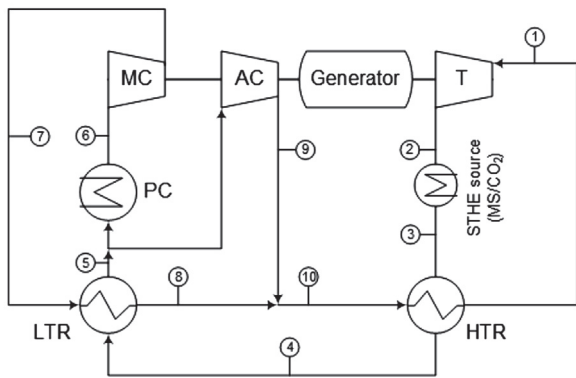
(b) Novel recompression cycle (RC-LP)

Fig. 1. Conventional (a) and novel (b) recompression cycle.

Fig. 2. Split expansion layout (adapted from [18]).

outlet, therefore reducing the recovering effect. The recompression cycle splits the recuperator into two units (LTR and HTR), using two compressors to use a lower mass flow rate in the stream with the higher specific heat. According with [39] the optimal split of the mass flow rate (split ratio, that is, the mass flow rate crossing the auxiliary compressor divided by the mass flow rate crossing the hot stream of the LTR) is that which achieves the same temperature approach at both extremes of the LTR (balanced heat exchanger).

It is observed how the AC inlet stream is taken upstream the pre-cooler, so the AC outlet reaches a high temperature, similar to the cold stream leaving the LTR, thus reducing the irreversibility in the mixing point (7-8-9 in Fig. 1a and 8-9-10 in Fig. 1b). Finally, the same mass flow rate is used in both streams of the HTR, due to the higher temperature reduces the difference in the specific heats. In Fig. 1a the molten salt (MS)/CO_2 heat exchanger would have to be a PCHE, in order to support the high pressure difference between both fluids (usually from 250 to 300 bar in the CO_2 versus 5 to 6 bar in the molten salt). However, in Fig. 1b a STHE heat exchanger can be used due to the low pressure in the CO_2 side (from 75 to 85 bar).

As it has been found in the literature [36], the use of STHE limits the turbine inlet pressure to 200 bar. Thus, if a PCHE is used, it should be designed with a hybrid configuration to avoid clogging issues in the salt channels [35], which also limits the turbine inlet pressure to 200 bar. This limitation is overcome with the proposed cycle. Higher cycle efficiencies are expected due to the fact that it increases with the turbine inlet pressure in the common range used in S-CO_2 [26]. However, in the proposed cycle, the turbine inlet temperature is reduced due to the use of the HTR as an intermediate heat exchanger between the molten salt and the CO_2. Consequently, a comprehensive assessment is required.

Another important feature of the proposed cycle, working at high turbine inlet pressure, is the higher density of the CO_2, which leads to
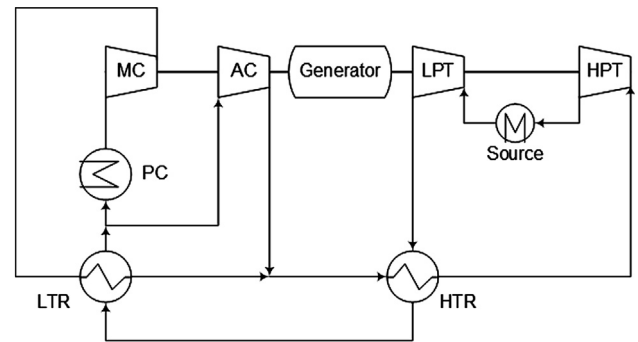
smaller sections in pipes, heat exchangers, and turbine. This increases the compactness of the layout, enhancing the dynamic response, which is an advantage for the grid stability, as found by Xu et al. [27]. The higher turbine inlet pressure also produces a greater area enclosed by the path of the cycle in the T-s diagram, which entails to a higher specific work. Finally, the design of the STHE with low pressure in the CO_2 tubes is expected to reduce the investment in this component.

The cycle rejects the heat power to the thermal sink through the pre-cooler (PC). Taking into account the site conditions in CSP technologies, two types of thermal sinks have been considered: wet cooling, which leads to a CO_2/water pre-cooler, and dry cooling which uses an air-cooled pre-cooler, a typical solution in arid sites.

In the proposed cycle, the heat power supply through the low pressure side is inspired in the so-called split expansion cycle [22], although in that case two turbines were used. In the simplest version of such cycle the heat power supply acts as a reheater, that is, supplying the heat power at an intermediate pressure. The flow downstream the low pressure turbine (LPT) transfers the heat power to the stream incoming to the high pressure turbine (HPT) in the HTR (Fig. 2). In this sense, the proposed layout supresses the low pressure turbine, delivering the heat power to the stream leaving the turbine (the low pressure side) and then transferring it to the stream incoming to the turbine by means of the HTR. In addition, Wang et al. [18] recommend the split expansion cycle to reduce thermal stress. Therefore, the objective is similar in the proposed cycle: to reduce the pressure load over the heat exchanger in order to replace the usually required PCHE by a STHE, which allows enough area to the molten salt to avoid thawing/clogging issues.

Four alternatives have been analysed, all of them based on recompression cycle. They include the aforementioned recompression (RC-LP), intercooling (RC-IC-LP), reheating (RC-RH-LP), and intercooling with reheating (RC-IC-RH-LP). For the sake of clarity, Fig. 3 shows these proposed layouts (b, d, f and h, respectively) together with conventional ones, designated without "-LP" (a, c, e and g, respectively).

2.2. Cycle modelling

Energy and mass balances have been applied to each component, together with specific equations, as isentropic efficiencies for turbomachines, temperature approaches and pressure drops for heat exchangers. In the following paragraphs, the model for each component is described, summarising the actual equations in Tables 1–4 according to the layouts given in Fig. 3.

Compressors are modelled as adiabatic, through the isentropic efficiency (η_c), as stated by equation (1), where "i" and "o" subscripts denote "inlet" and "outlet" conditions, respectively; "h" is the enthalpy of the CO_2, "s" the entropy and "p" the pressure. The energy balance leads to equation (2) to obtain the power consumption ($\dot{W}_C$), where $\dot{m}_c$ stands for the mass flow rate of the compressor.
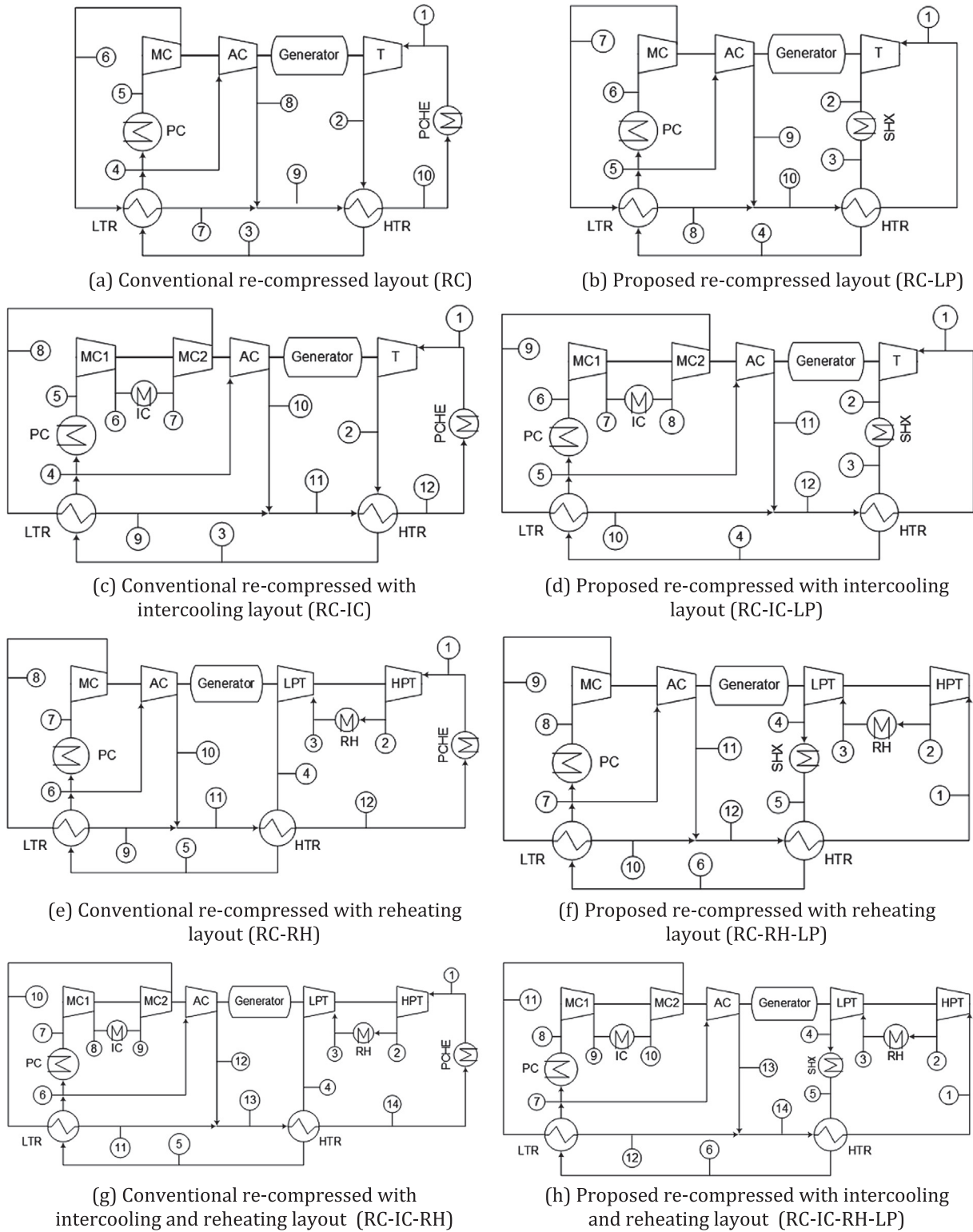
(a) Conventional re-compressed layout (RC)

(b) Proposed re-compressed layout (RC-LP)

(c) Conventional re-compressed with intercooling layout (RC-IC)

(d) Proposed re-compressed with intercooling layout (RC-IC-LP)

(e) Conventional re-compressed with reheating layout (RC-RH)

(f) Proposed re-compressed with reheating layout (RC-RH-LP)

(g) Conventional re-compressed with intercooling and reheating layout (RC-IC-RH)

(h) Proposed re-compressed with intercooling and reheating layout (RC-IC-RH-LP)

Fig. 3. Analysed layouts in conventional (a, c, e and g) and proposed (b, d, f and h) arrangements.

$$\eta_c = \frac{h_{os} - h_i}{h_o - h_i}; \quad h_{os} = h(s_i; p_o) \tag{1}$$

$$\dot{W}_C = \dot{m}_c \cdot (h_o - h_i) \tag{2}$$

Main compressor inlet conditions have been taken as 85 bar and 35 °C, or 50 °C. This pressure allows to reach a reasonable trade-off between closeness to critical point and compressor instability issues, if any [40]. The chosen values for the inlet temperature depend on the cooling system: 35 °C for wet cooling and 50 °C for dry cooling [19]. Intercooling pressures have been also optimised to maximise the cycle efficiency, being the MC2 inlet temperature the same than that of the MC1. Isentropic efficiency in compressors has been set to 88%, according to [41].

Turbines are modelled as adiabatic, through the isentropic efficiency (η_T), as stated by equation (3). The energy balance leads to the equation (4) to obtain the produced power ($\dot{W}_T$), where $\dot{m}_T$ stands for the

Table 1
Cycle modelling of basic recompression layouts.

	RC-LP	RC
MC	$\dot{W}_{MC} = \dot{m}\cdot(1-\alpha)\cdot(h_7 - h_6)$	$\dot{W}_{MC} = \dot{m}\cdot(1-\alpha)\cdot(h_6 - h_5)$
AC	$\dot{W}_{AC} = \dot{m}\cdot\alpha\cdot(h_9 - h_5)$	$\dot{W}_{AC} = \dot{m}\cdot\alpha\cdot(h_8 - h_4)$
T	$\dot{W}_T = \dot{m}\cdot(h_1 - h_2)$	$\dot{W}_T = \dot{m}\cdot(h_1 - h_2)$
Source heat exchanger	$\dot{Q}_{SHX} = \dot{m}\cdot(h_3 - h_2)$	$\dot{Q}_{PCHE} = \dot{m}\cdot(h_1 - h_{10})$
	$\Delta p_{CO2} = p_2 - p_3$	$\Delta p_{CO2} = p_{10} - p_1$
	$PP_{SHX} = T_{so} - T_2$	$PP_{SHX} = T_{so} - T_{10}$
	$PP_{SHX} = T_{si} - T_3$	$PP_{SHX} = T_{si} - T_1$
HTR	$\dot{Q}_{HTR} = \dot{m}\cdot(h_3 - h_4)$	$\dot{Q}_{HTR} = \dot{m}\cdot(h_2 - h_3)$
	$h_3 - h_4 = h_1 - h_{10}$	$h_2 - h_3 = h_{10} - h_9$
	$\Delta p_{CO2} = p_3 - p_4$	$\Delta p_{CO2} = p_2 - p_3$
	$\Delta p_{CO2} = p_{10} - p_1$	$\Delta p_{CO2} = p_9 - p_{10}$
	$PP_{HTR} = T_4 - T_{10}$	$PP_{HTR} = T_3 - T_9$
LTR	$\dot{Q}_{LTR} = \dot{m}\cdot(h_4 - h_5)$	$\dot{Q}_{LTR} = \dot{m}\cdot(h_3 - h_4)$
	$h_4 - h_5 = \alpha\cdot(h_8 - h_7)$	$h_3 - h_4 = \alpha\cdot(h_7 - h_6)$
	$\Delta p_{CO2} = p_4 - p_5$	$\Delta p_{CO2} = p_3 - p_4$
	$\Delta p_{CO2} = p_7 - p_8$	$\Delta p_{CO2} = p_6 - p_7$
	$PP_{LTR} = T_4 - T_8$	$PP_{LTR} = T_3 - T_7$
	$PP_{LTR} = T_5 - T_7$	$PP_{LTR} = T_4 - T_6$
PC	$\dot{Q}_{PC} = \dot{m}\cdot\alpha\cdot(h_5 - h_6)$	$\dot{Q}_{PC} = \dot{m}\cdot\alpha\cdot(h_4 - h_5)$
Junction	$p_8 = p_9 = p_{10}$	$p_8 = p_9 = p_7$
	$\alpha\cdot h_8 + (1-\alpha)\cdot h_9 = h_{10}$	$\alpha\cdot h_7 + (1-\alpha)\cdot h_8 = h_9$

Table 2
Cycle modelling of recompression with intercooling layouts.

	RC-IC-LP	RC-IC
MC1	$\dot{W}_{MC1} = \dot{m}\cdot(1-\alpha)\cdot(h_7 - h_6)$	$\dot{W}_{MC1} = \dot{m}\cdot(1-\alpha)\cdot(h_6 - h_5)$
MC2	$\dot{W}_{MC2} = \dot{m}\cdot(1-\alpha)\cdot(h_9 - h_8)$	$\dot{W}_{MC2} = \dot{m}\cdot(1-\alpha)\cdot(h_8 - h_7)$
AC	$\dot{W}_{AC} = \dot{m}\cdot\alpha\cdot(h_{11} - h_5)$	$\dot{W}_{AC} = \dot{m}\cdot\alpha\cdot(h_{10} - h_4)$
T	$\dot{W}_T = \dot{m}\cdot(h_1 - h_2)$	$\dot{W}_T = \dot{m}\cdot(h_1 - h_2)$
Source heat exchanger	$\dot{Q}_{SHX} = \dot{m}\cdot(h_3 - h_2)$	$\dot{Q}_{PCHE} = \dot{m}\cdot(h_1 - h_{12})$
	$\Delta p_{CO2} = p_2 - p_3$	$\Delta p_{CO2} = p_{12} - p_1$
	$PP_{SHX} = T_{so} - T_2$	$PP_{SHX} = T_{so} - T_{12}$
	$PP_{SHX} = T_{si} - T_3$	$PP_{SHX} = T_{si} - T_1$
HTR	$\dot{Q}_{HTR} = \dot{m}\cdot(h_3 - h_4)$	$\dot{Q}_{HTR} = \dot{m}\cdot(h_2 - h_3)$
	$h_3 - h_4 = h_1 - h_{12}$	$h_2 - h_3 = h_{12} - h_{11}$
	$\Delta p_{CO2} = p_3 - p_4$	$\Delta p_{CO2} = p_2 - p_3$
	$\Delta p_{CO2} = p_{12} - p_1$	$\Delta p_{CO2} = p_{11} - p_{12}$
	$PP_{HTR} = T_4 - T_{12}$	$PP_{HTR} = T_3 - T_{11}$
LTR	$\dot{Q}_{LTR} = \dot{m}\cdot(h_4 - h_5)$	$\dot{Q}_{LTR} = \dot{m}\cdot(h_3 - h_4)$
	$h_4 - h_5 = \alpha\cdot(h_{10} - h_9)$	$h_3 - h_4 = \alpha\cdot(h_9 - h_8)$
	$\Delta p_{CO2} = p_4 - p_5$	$\Delta p_{CO2} = p_3 - p_4$
	$\Delta p_{CO2} = p_9 - p_{10}$	$\Delta p_{CO2} = p_8 - p_9$
	$PP_{LTR} = T_4 - T_{10}$	$PP_{LTR} = T_3 - T_9$
	$PP_{LTR} = T_5 - T_9$	$PP_{LTR} = T_4 - T_8$
PC	$\dot{Q}_{PC} = \dot{m}\cdot\alpha\cdot(h_5 - h_6)$	$\dot{Q}_{PC} = \dot{m}\cdot\alpha\cdot(h_4 - h_5)$
IC	$\dot{Q}_{IC} = \dot{m}\cdot\alpha\cdot(h_7 - h_8)$	$\dot{Q}_{IC} = \dot{m}\cdot\alpha\cdot(h_6 - h_7)$
Junction	$p_{11} = p_{12} = p_{10}$	$p_{10} = p_9 = p_{11}$
	$\alpha\cdot h_{10} + (1-\alpha)\cdot h_{11} = h_{12}$	$\alpha\cdot h_9 + (1-\alpha)\cdot h_{10} = h_{11}$

Table 3
Cycle modelling of recompression with reheating layouts.

	RC-RH-LP	RC-RH
MC	$\dot{W}_{MC} = \dot{m}\cdot(1-\alpha)\cdot(h_9 - h_8)$	$\dot{W}_{MC} = \dot{m}\cdot(1-\alpha)\cdot(h_8 - h_7)$
AC	$\dot{W}_{AC} = \dot{m}\cdot\alpha\cdot(h_{11} - h_7)$	$\dot{W}_{AC} = \dot{m}\cdot\alpha\cdot(h_{10} - h_6)$
HPT	$\dot{W}_{HPT} = \dot{m}\cdot(h_1 - h_2)$	$\dot{W}_{HPT} = \dot{m}\cdot(h_1 - h_2)$
LPT	$\dot{W}_{LPT} = \dot{m}\cdot(h_3 - h_4)$	$\dot{W}_{LPT} = \dot{m}\cdot(h_3 - h_4)$
Source heat exchanger	$\dot{Q}_{SHX} = \dot{m}\cdot(h_5 - h_4)$	$\dot{Q}_{PCHE} = \dot{m}\cdot(h_1 - h_{12})$
	$\Delta p_{CO2} = p_4 - p_5$	$\Delta p_{CO2} = p_{12} - p_1$
	$PP_{SHX} = T_{soS} - T_4$	$PP_{SHX} = T_{soS} - T_{12}$
	$PP_{SHX} = T_{si} - T_5$	$PP_{SHX} = T_{si} - T_1$
RH	$\dot{Q}_{RH} = \dot{m}\cdot(h_3 - h_2)$	$\dot{Q}_{RH} = \dot{m}\cdot(h_3 - h_2)$
	$\Delta p_{CO2} = p_2 - p_3$	$\Delta p_{CO2} = p_2 - p_3$
	$PP_{RH} = T_{soR} - T_2$	$PP_{RH} = T_{soR} - T_2$
	$PP_{RH} = T_{si} - T_3$	$PP_{RH} = T_{si} - T_3$
HTR	$\dot{Q}_{HTR} = \dot{m}\cdot(h_5 - h_6)$	$\dot{Q}_{HTR} = \dot{m}\cdot(h_4 - h_5)$
	$h_5 - h_6 = h_1 - h_{12}$	$h_4 - h_5 = h_{12} - h_{11}$
	$\Delta p_{CO2} = p_5 - p_6$	$\Delta p_{CO2} = p_4 - p_5$
	$\Delta p_{CO2} = p_{12} - p_1$	$\Delta p_{CO2} = p_{11} - p_{12}$
	$PP_{HTR} = T_5 - T_{12}$	$PP_{HTR} = T_4 - T_{11}$
LTR	$\dot{Q}_{LTR} = \dot{m}\cdot(h_6 - h_7)$	$\dot{Q}_{LTR} = \dot{m}\cdot(h_5 - h_6)$
	$h_6 - h_7 = \alpha\cdot(h_{10} - h_9)$	$h_5 - h_6 = \alpha\cdot(h_9 - h_8)$
	$\Delta p_{CO2} = p_6 - p_7$	$\Delta p_{CO2} = p_5 - p_6$
	$\Delta p_{CO2} = p_9 - p_{10}$	$\Delta p_{CO2} = p_8 - p_9$
	$PP_{LTR} = T_6 - T_{10}$	$PP_{LTR} = T_5 - T_9$
	$PP_{LTR} = T_7 - T_9$	$PP_{LTR} = T_6 - T_8$
PC	$\dot{Q}_{PC} = \dot{m}\cdot\alpha\cdot(h_7 - h_8)$	$\dot{Q}_{PC} = \dot{m}\cdot\alpha\cdot(h_6 - h_7)$
Junction	$p_{11} = p_{12} = p_{10}$	$p_{10} = p_9 = p_{11}$
	$\alpha\cdot h_{10} + (1-\alpha)\cdot h_{11} = h_{12}$	$\alpha\cdot h_9 + (1-\alpha)\cdot h_{10} = h_{11}$

Table 4
Cycle modelling of recompression with intercooling and reheating layouts.

	RC-IC-RH-LP	RC-IC-RH
MC1	$\dot{W}_{MC1} = \dot{m}\cdot(1-\alpha)\cdot(h_9 - h_8)$	$\dot{W}_{MC1} = \dot{m}\cdot(1-\alpha)\cdot(h_8 - h_7)$
MC2	$\dot{W}_{MC2} = \dot{m}\cdot(1-\alpha)\cdot(h_{11} - h_{10})$	$\dot{W}_{MC2} = \dot{m}\cdot(1-\alpha)\cdot(h_{10} - h_9)$
AC	$\dot{W}_{AC} = \dot{m}\cdot\alpha\cdot(h_{13} - h_7)$	$\dot{W}_{AC} = \dot{m}\cdot\alpha\cdot(h_{12} - h_6)$
HPT	$\dot{W}_{HPT} = \dot{m}\cdot(h_1 - h_2)$	$\dot{W}_{HPT} = \dot{m}\cdot(h_1 - h_2)$
LPT	$\dot{W}_{LPT} = \dot{m}\cdot(h_3 - h_4)$	$\dot{W}_{LPT} = \dot{m}\cdot(h_3 - h_4)$
Source heat exchanger	$\dot{Q}_{SHX} = \dot{m}\cdot(h_5 - h_4)$	$\dot{Q}_{PCHE} = \dot{m}\cdot(h_1 - h_{14})$
	$\Delta p_{CO2} = p_4 - p_5$	$\Delta p_{CO2} = p_{14} - p_1$
	$PP_{SHX} = T_{soS} - T_4$	$PP_{SHX} = T_{soS} - T_{14}$
	$PP_{SHX} = T_{si} - T_5$	$PP_{SHX} = T_{si} - T_1$
RH	$\dot{Q}_{RH} = \dot{m}\cdot(h_3 - h_2)$	$\dot{Q}_{RH} = \dot{m}\cdot(h_3 - h_2)$
	$\Delta p_{CO2} = p_2 - p_3$	$\Delta p_{CO2} = p_2 - p_3$
	$PP_{RH} = T_{soR} - T_2$	$PP_{RH} = T_{soR} - T_2$
	$PP_{RH} = T_{si} - T_3$	$PP_{RH} = T_{si} - T_3$
HTR	$\dot{Q}_{HTR} = \dot{m}\cdot(h_5 - h_6)$	$\dot{Q}_{HTR} = \dot{m}\cdot(h_4 - h_5)$
	$h_5 - h_6 = h_1 - h_{14}$	$h_4 - h_5 = h_{14} - h_{13}$
	$\Delta p_{CO2} = p_5 - p_6$	$\Delta p_{CO2} = p_4 - p_5$
	$\Delta p_{CO2} = p_{14} - p_1$	$\Delta p_{CO2} = p_{13} - p_{14}$
	$PP_{HTR} = T_6 - T_{14}$	$PP_{HTR} = T_5 - T_{13}$
LTR	$\dot{Q}_{LTR} = \dot{m}\cdot(h_6 - h_7)$	$\dot{Q}_{LTR} = \dot{m}\cdot(h_5 - h_6)$
	$h_6 - h_7 = \alpha\cdot(h_{12} - h_{11})$	$h_5 - h_6 = \alpha\cdot(h_{11} - h_{10})$
	$\Delta p_{CO2} = p_6 - p_7$	$\Delta p_{CO2} = p_5 - p_6$
	$\Delta p_{CO2} = p_{11} - p_{12}$	$\Delta p_{CO2} = p_{10} - p_{11}$
	$PP_{LTR} = T_6 - T_{12}$	$PP_{LTR} = T_5 - T_{11}$
	$PP_{LTR} = T_7 - T_{11}$	$PP_{LTR} = T_6 - T_{10}$
PC	$\dot{Q}_{PC} = \dot{m}\cdot\alpha\cdot(h_7 - h_8)$	$\dot{Q}_{PC} = \dot{m}\cdot\alpha\cdot(h_6 - h_7)$
IC	$\dot{Q}_{IC} = \dot{m}\cdot\alpha\cdot(h_9 - h_{10})$	$\dot{Q}_{IC} = \dot{m}\cdot\alpha\cdot(h_8 - h_9)$
Junction	$p_{13} = p_{12} = p_{14}$	$p_{11} = p_{12} = p_{13}$
	$\alpha\cdot h_{12} + (1-\alpha)\cdot h_{13} = h_{14}$	$\alpha\cdot h_{11} + (1-\alpha)\cdot h_{12} = h_{13}$

mass flow rate of the turbine.

$$\eta_T = \frac{h_i - h_o}{h_i - h_{os}}; \quad h_{os} = h(s_i; p_o) \tag{3}$$

$$\dot{W}_T = \dot{m}_T\cdot(h_i - h_o) \tag{4}$$

The turbine inlet pressure has been taken as a parameter to obtain the cycle efficiency, being 300 bar the maximum allowable value. The turbine inlet temperature depends on the HTR operation, establishing a value of 688 °C as the maximum CO_2 temperature (at the CO_2 outlet of the source STHX). Reheating pressures have been optimised to maximise the cycle efficiency, being the LPT inlet temperature the same than that of the HPT. Isentropic efficiency in the turbine has been set to 92%, according to [41].

Energy balance has been also applied to the source/reheating and sink heat exchangers through the heat duty, in order to relate the mass flow rate of both streams (molten salt/CO_2 in the source/reheating heat exchanger and CO_2/water or CO_2/air in the sink heat exchanger). The molten salt inlet temperature is 700 °C. The cooling medium comes into the heat exchanger at 25 °C (water) or 35 °C (air) and leaves it at 35 °C (water) or 60 °C (air), being the inlet temperatures common for the

design point [19]. The outlet temperatures are chosen to reduce the cooling medium mass flow rate. Equation (5) is adopted for source/reheating heat exchangers (SC/RH) and equation (6) for precooler/intercooler heat exchangers (PC/IC). Both source and reheating heat exchangers have been considered balanced, with an approach temperature between 10 °C and 12 °C.

$$\dot{Q}_{SC/RH} = \dot{m}_{SC/RH} \cdot (h_o - h_i) \qquad (5)$$

$$\dot{Q}_{PC/IC} = \dot{m}_{PC/IC} \cdot (h_i - h_o) \qquad (6)$$

At recuperators (HTR and LTR), the energy balance is applied in a specific way, as stated in equation (7) for HTR and in equation (8) for LTR, where "c" and "h" subscripts stand for "cold" and "hot" streams and "α" stands for the ratio of cold to hot mass flow rate streams at LTR. As it has been commented previously, this ratio is adjusted to balance the LTR. Minimum approach temperature is set to 5 °C at LTR and 10 °C at HTR, taking into account the large amount of heat duty in the HTR (it transfers the thermal energy from the source to the cycle and performs as a recuperator, too) and the unbalance operation due to the different specific heats [39].

$$h_{hi} - h_{ho} = h_{co} - h_{ci} \qquad (7)$$

$$h_{hi} - h_{ho} = \alpha \cdot (h_{co} - h_{ci}) \qquad (8)$$

Pressure drop in the CO_2 stream of the heat exchangers has been taken as 40 kPa [42]. In the case of molten salt, a maximum velocity of 3 m/s has been selected, according to [43]. No pressure drops have been considered in pipes inside the cycle, but an overall value of 5 bar has been assumed in the heat source (molten salt) and heat sink (water in wet cooling case) loops.

Finally, in the junction of the main compressor/s and auxiliary compressor streams, no pressure drop is assumed and the energy balance leads to equation (9), where "mix" subscript stands for the mixture state.

$$\alpha \cdot h_{LTR;co} + (1 - \alpha) \cdot h_{AC;o} = h_{mix} \qquad (9)$$

Three power outputs are defined: cycle, gross and net. Cycle power is the difference between the total power generated by the turbines and the consumed by the compressors (equation (10)). Gross power is the result of considering the generator efficiency (η_g), taken as 97% [44] over the cycle power (equation (11)), and net power is obtained subtracting the heat source and heat sink loop pumping consumptions to the gross power (equation (12)). In the case of dry cooling (both precooler and intercooler, if any), 50 kW has been assumed for each electric engine. This value is expected to be lower than the pumps consumption in the wet scenario, in order to compensate the lower efficiency caused by the dry cooling.

$$\dot{W}_{cycle} = \dot{W}_{T,HPT} + \dot{W}_{T,LPT} - \dot{W}_{MC,MC1} - \dot{W}_{MC2} - \dot{W}_{AC} \qquad (10)$$

$$\dot{W}_{gross} = \dot{W}_{cycle} \cdot \eta_g \qquad (11)$$

$$\dot{W}_{net} = \dot{W}_{gross} - \dot{W}_{HTP} - \dot{W}_{LTP} - \dot{W}_{CP} \qquad (12)$$

A cycle power output of 50 MW has been assumed, taking into account the usual range from 10 MWe for first prototypes to 100 MWe for commercial plants [1]. The cycle efficiency takes into account the cycle power and the heat transferred to the cycle by the STHXs (SHX and RH, if any).

2.3. Fluid properties

Carbon dioxide, water and air have been modelled as pure substances, using the correlations given in Engineering Equation Solver (EES, [45]) software. The whole cycle model has been implemented in this software to couple the equations of the properties with the components. This software is also capable of optimising the cycle efficiency in order to obtain the intercooling and reheating pressures, as explained

Table 5
Correlations for salt properties.

Property	Correlation	Reference
Specific heat [J/kg-K]	1180	[6]
Density [kg/m³]	$1899.3 - 0.43 \cdot T$ [°C]	[5]
Conductivity [W/m-K]	$0.5423 - 0.0002 \cdot T$ [°C]	[5]
Dynamic viscosity [Pa·s]	$8.25 \cdot 10^{-6} \cdot e^{11,874.71735/(1350.84595+T) [°C]}$	[5]

before. A chloride ternary salt (weight composition: 24.5% NaCl – 20.5% KCl – 55.0% MgCl₂) has been selected as molten salt due to its allowable operating range (387 °C to more than 800 °C), low volumetric heat capacity (ρ·c = 1.9 J/cm³-K) and cost (295 $/tonne) [6]. Table 5 gives the correlations for the properties of the salt.

According with Mohan et al. [6], this salt exhibits advantages over other options with good stability at high temperatures. So, ternary carbonate mixtures present good physical properties, but they are too expensive due to the presence of Li₂CO₃. Chlorides also exhibit good physical properties, having being used as coolants in nuclear power plants. Among them, those containing ZnCl₂, the so-called NaKZn-Cl ternary salts, should be discarded due to the high cost of the ZnCl₂. Finally, the 24.5% NaCl – 20.5% KCl – 55.0% MgCl₂ selected combines good physical properties and low cost, as was stated in Section 1. Mohan et al. [6] proposed this salt as the most promising candidate, although it demands future researches to investigate potential corrosion concerns of the chloride salts. In the current work, this issue has been taken into account from the NREL Gen3 Demonstration Roadmap [1], where alloy 347 is considered for the cold tank and Haynes 230 for the hot tank, both containing a chloride salt.

2.4. Model of heat exchangers

In PCHEs (LTR, HTR in both cooling scenarios and PC in wet cooling scenario), at least one of the streams is CO_2, whose properties are strongly dependent on temperature and pressure, especially close to the critical point. So, in such heat exchangers an iterative procedure has been implemented dividing the length of the heat exchanger in elements and assuming a continuous variation of the properties [46]. Specific correlations have been developed for CO_2 convection heat transfer coefficients, which can be found in [47]. For the current analysis, recommendations from Dostal [17] have been followed. PCHE dimensions have been obtained from Heatric [29], taking into account its manufacturing limitations. The manufacturing is modular, with maximum dimensions of a module (width × length × height) of 0.6 m × 0.6 m × 1.5 m, and being the height the flow path of the streams. Each module contains 96,000 channels (48,000 for each stream). Up to 14 modules can be piled up in parallel in a bonding structure, so constituting the biggest stack (8.4 m long). The inner channels are semi-circular, with 2 mm diameter and 2.5 mm pitch. Each layer of channels is 1.5 mm wide.

Initially, the overall heat transfer duty is equally divided, so fixing the heat transfer for each element. The overall heat transfer coefficient (U_i) of the i-th element is obtained with the convection heat transfer coefficients at each stream and the thermal conductance, per unit heat transfer area, between the channels (29.2 kW/m²-K for SS 316 and 45 kW/m²-K for Inconel 617 taking into account 0.5 mm thickness and thermal conductivitys of 14.6 W/m-K and 22.5 W/m-K, respectively). The heat transfer ($\dot{Q}_i$), in the i-th element, is assessed with equation (13) where the heat transfer area is expressed as the wetted perimeter (P_i) times the length (L_i). Dostal recommendations [17] include the Darcy friction factor (f_i), so it is possible to calculate the pressure drop of the i-th element (Δp_i), equation (14), where D_i stands for the hydraulic diameter of the channel, c_i is the mean velocity of the fluid and ρ_i is the density. Then, the iterative procedure starts, with the assumption of a certain number of channels, finishing when the desired temperatures at

each ports are reached. The total length of the heat exchanger and total pressure drops at each stream are obtained. If the maximum pressure drop between both streams is greater than the prescribed one, the procedure is repeated with more tubes, until the largest pressure drop coincides with the prescribed one for that stream (in the other stream a pressure drop lower than the prescribed one is obtained, due to the same length of hot and cold channels). On the contrary, if the maximum pressure drop is lower than the prescribed one, the number of channels is reduced in order to avoid an oversized heat exchanger. As an example, Fig. 4 shows the temperature profile, and Fig. 5 the heat transfer coefficients at each stream and the overall heat transfer coefficient at the LTR in the RC-IC-RH-LP layout (dry cooling). The total number of channels (both hot and cold streams) is 1,496,000, with a flow path (height of the heat exchanger) of 3.37 m (three heat exchangers should be arranged in serial). This leads to 46.75 modules, so obtaining a length of the heat exchanger of 4.68 m arranging two stacks in parallel.

$$\dot{Q}_i = U_i \cdot L_i \cdot P_i \cdot (T_{h;i} - T_{c;i}) \tag{13}$$

$$\Delta p_i = f_i \cdot \left(\frac{L_i}{D_i}\right) \cdot \rho_i \cdot \left(\frac{c_i^2}{2}\right) \tag{14}$$

Pre-cooler and intercooler, in the case of dry cooling, are air coolers -cross flow heat exchangers. A core sCF-734 has been used. The air side has been modelled with the correlations implemented in EES. The air length is controlled to obtain a fan consumption lower than 50 kW. The number of tubes is controlled to obtain a pressure drop lower than 40 kPa. In the CO_2 side, the same discretisation procedure than in the PCHEs has been used, due to the proximity of this stream to the critical point in these heat exchangers.

As stated above, in the novel proposed layout, the use of conventional shell and tube heat exchangers is possible thanks to the lower pressure load in the source and in the reheater. The primary fluid entering the shell is the ternary chloride molten salt and the secondary fluid going through the tubes is CO_2. For the thermofluidynamic model, the heat transfer to the CO_2 in the tubes is calculated using the Gnielinski correlation, and the pressure drop by the Darcy-Weisbach equation [48]. Averaged CO_2 properties are considered in this case, as the working temperatures are far from the critical point. For the molten salt in the shell, it is suggested to use the McAdams correlation to calculate the heat transfer, and the Kern method to determine the

pressure drop [48].

The material used for both the tubes and the shell is a high-nickel alloy, Inconel 625, which is recommended in terms of compatibility and cost [1]. All these STHXs have been modelled as counterflow heat exchangers with one shell pass and one tube pass. Regarding the shell type, an "E" shell has been chosen according to Tubular Exchanger Manufacturers Association (TEMA) standards [49]. The minimum tube thickness has been calculated according to ASME (American Society of Mechanical Engineers) Boiling and Pressure Vessel Code [50]; based on this lower limit, it has been selected a standardized wall thickness, in terms of the Birmingham Wire Gage (BWG) of the tube. Other manufacturing requirements of this type of heat exchangers have been considered, as the shell-diameter-to-tube-length ratio, which should be within the limits of 1/5 to 1/15. Besides, maximum tube length is limited by architectural layouts and by transportation to about 30 m.

As an example, Table 6 shows the detailed results of the source heat exchanger of the RC-IC-RH-LP layout (dry cooling). As in the shell and tube heat exchangers no discretisation process has been carried out, no variation of the heat transfer coefficients along the length is obtained.

2.5. Heat source and heat sink

2.5.1. Heating and cooling loops

Fig. 6 shows both heating and cooling loops. The heating loop includes both source (SHX) and reheating (RH) heat exchangers (if required), of shell and tube type. One pump (HTP) removes the molten salt mass flow rate from the hot tank and another pump (LTP) from the cold tank. A solar multiple of 1.5 has been assumed, so the mass flow rate in the LTP is 1.5 times the one in the HTP. Both pumps are assumed with an efficiency of 75% (it is a conservative value and the consumption is expected to be lower). The required salt inventory assumes 10% of unusable residuals at the bottom of the tank for the pump suction head. Finally, the volume tank considers 10% of freeboard above the full-salt level [1]. Fig. 6 shows the cooling loop in wet cooling scenario. If dry cooling is selected, PC and IC would be air cooled heat exchangers and the fan consumption would come from its electrical engine. An efficiency of 75% has been assumed for the cooling pump (CP) or the fans (dry cooling) again. An overall head of 5 bar is assumed for all the pumps (conservative value). The storage time has been taken as 3 h, with 6 h of charge period (both assumed as equivalent at full
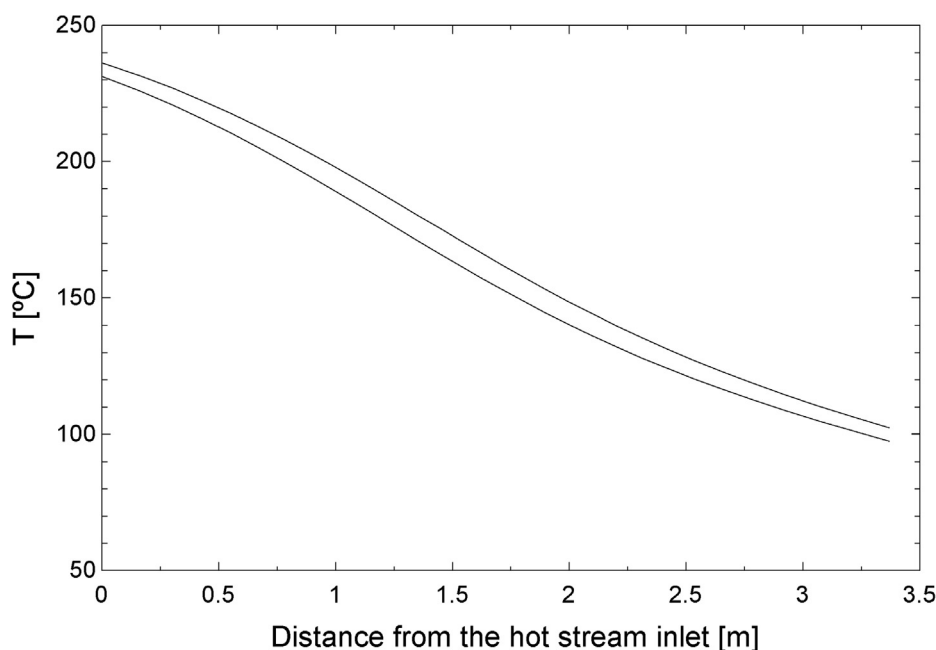

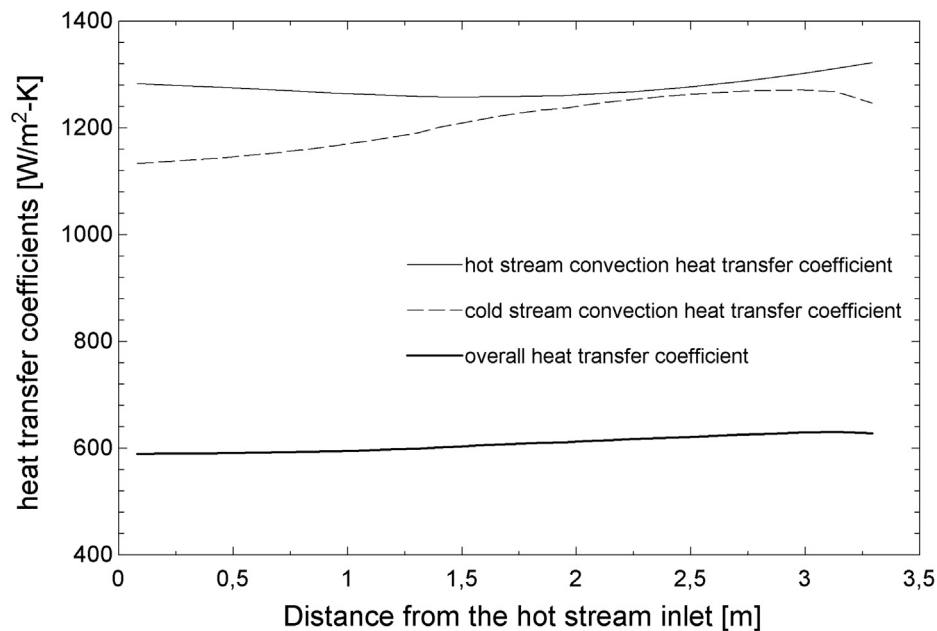**Fig. 4.** Temperature profile of LTR in the RC-IC-RH-LP layout (dry cooling).

Fig. 5. Heat transfer coefficients along the LTR in the RC-IC-RH-LP layout (dry cooling).

Table 6
Dimensions of source heat exchanger (shell and tubes) in RCIC-RH-LP (dry cooling) layout.

Thermal characteristics	
Thermal power (MWth)	45.944
Overall Heat Transfer Coefficient (W/m² - °C)	328.88
Sizing and geometrical characteristics	
Number of units	1
Tube dimensional data (normalized)	3/4″ BWG Gauge 10
Outer diameter (mm)	19.05
Thickness (mm)	3.404
Tube pitch size (mm)	23.81
Baffle spacing (m)	2
Pitch-Tube layout	Triangular
Number of tube passes	1
Number of shell passes	1
Number of tubes	10,315
Heat transfer area (m²)	10319.78
Length (m)	16.72
Shell diameter (m)	2.88
Primary fluid (molten salt)	
Maximum velocity (m/s)	3
Primary inlet temperature (°C)	700
Primary inlet pressure (bar)	6
Primary mass flow rate (kg/s)	389.3
Primary outlet temperature (°C)	600
Primary outlet pressure (bar)	5.70
Primary pressure drop (bar)	0.295
Convection heat transfer coefficient (tube side) (W/m² - K)	1238.45
Fouling Resistance (m² -K/W)	0.000088
Secondary fluid (CO$_2$)	
Maximum velocity (m/s)	6
Secondary inlet temperature (°C)	584.8
Secondary inlet pressure (bar)	86.6
Secondary mass flow rate (kg/s)	361.96
Secondary outlet temperature (°C)	688
Secondary outlet pressure (bar)	86.20
Secondary pressure drop	0.402
Convection heat transfer coefficient (Shell side) (W/m² - K)	919.16
Fouling Resistance (m² -K/W)	0.000176

load). The temperature of the hot tank is 700 °C, depending on the temperature of the cold tank of the power cycle.

2.5.2. Receiver and heliostat field

As previously described in the introduction, a tubular cavity-type configuration has been selected for the receiver. Cavity receivers present lower radiation heat loss and higher convective heat loss than external receivers [51], so they seem to be the best option when the working temperature increases and the radiation heat loss becomes critical.

As can be seen in Fig. 7, the receiver consists of four panels. The fluid flow layout has been divided in two symmetrical circuits. The molten salt goes into the receiver through both side panels of the absorber surface, the lowest temperature zone in the receiver, and then is circulated to the central panels, to finally leave through the highest temperature region. This flow distribution improves the heat transfer, as it reduces the temperature difference between the absorber surface and the molten salt. Other thermal and geometric parameters of the receiver, i.e. the tube diameter, the aspect ratio, have been chosen or calculated according to technical literature, from classical handbooks [51] to design guides [52]. The maximum allowable concentrated flux has been taken from [53], and the general methodology has been checked with current studies [54].

All receivers have been designed to provide the heat power required for each cycle configuration. For all of them, the average MS velocity inside the tubes has been set to 1.6 m/s, thus ensuring an adequate comparison framework for the same cooling conditions. Since the inlet and outlet MS temperatures are different in each layout, as well as the mass flow, the tube diameters have been changed to meet the velocity value requirement.

The thermal model developed for the receiver introduces two main improvements, compared to other models in the literature that study the thermal performance [55] and include sensitivity analysis [56]. On the one hand, it takes into account the solar and infrared radiosity exchange inside the cavity, applying the semi-gray approximation to an enclosure, as the aperture is considered a "virtual" surface [57]. On the other hand, it calculates the convection heat loss from each of the panels of the receiver, applying the Clausing equation, which gives more accurate results than other more simplified equations [58]. In the end, the receiver performance obtained with this model matches the values
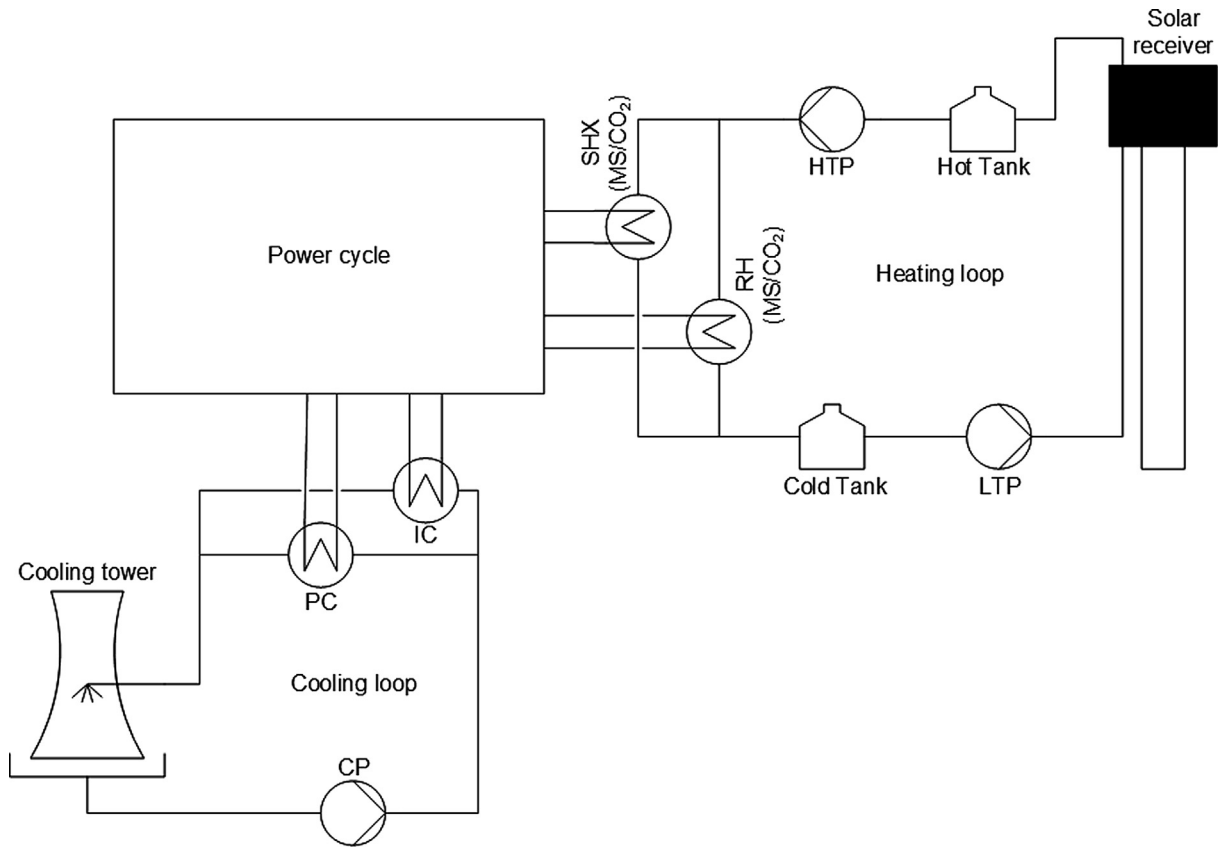
Fig. 6. Heating and cooling loops.

showed in bibliography for cavity receivers working at these higher temperatures [59]. Basic equations for this model are summarized below. The semi-gray theory applied to an enclosure is described by equations (15) and (16).

$$J_i^s (W/m^2) = (1 - \varepsilon_i^s) \cdot \left[G_i + \sum_j J_j^s \cdot F_{ij} \right]$$

(15)

$$J_i^r (W/m^2) = \varepsilon_i^r \cdot \sigma \cdot T_i^4 + (1 - \varepsilon_i^r) \cdot \sum_j J_j^r \cdot F_{ij}$$

(16)

In these equations, sub-indexes i/j refers to the surface of the cavity, and super-indexes s/r stands for the solar/infrared radiosity; J (W/m^2) is the radiosity from each surface; G (W/m^2) is the concentrated solar flux impinging each active panel of the receiver; F_{ij} is the view factor

from surface i to surface j; ε is the emissivity of each surface; T (K) is the temperature of each surface; and $\sigma = 5.67 \cdot 10^{-8}$ W/m^2-K^4 is the Stefan-Boltzmann constant.

This equations system is completed with other equation (17) describing the energy balance applied to each of the receiver surfaces.

$$\dot{q}_{useful,i} (W/m^2) = \sum_j (J_j^s \cdot F_{ij} + G_j \cdot \delta_{ji} - \delta_{ji} \cdot J_j^s) + \sum_j (J_j^r \cdot F_{ij} - \delta_{ji} \cdot J_j^r)$$

(17)

In this equation, $\dot{q}_{useful}$ is the useful heat from each surface, that is, the heat transferred to the molten salt flowing through the tubes by convection, and it is calculated using Gnielinski correlation [48]; and δ_{ij} is the Kronecker delta. It is important to point out that only the active surfaces present a useful heat $\dot{q}_{useful}$ and an incident solar flux G.

The heat losses from the receiver are described by equations
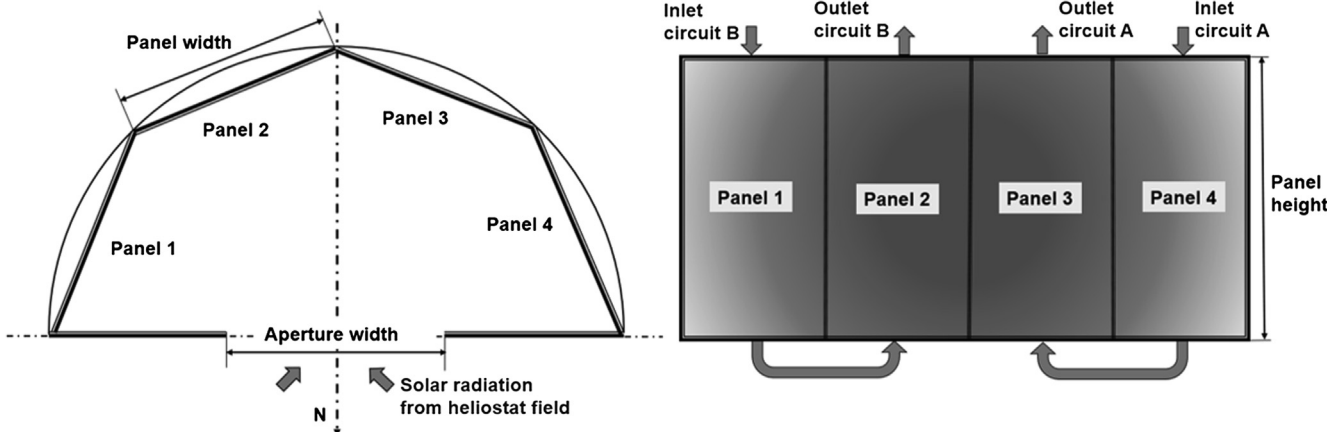
Fig. 7. Receiver cross-section view (left) and fluid flow configuration in the absorber surface (right).

(18)–(20). The total radiation heat loss is the sum of the solar and infrared radiosity leaving each surface (19). In the case of the aperture, being a virtual surface, both radiosities are null. As said above, convection heat loss is calculated by Clausing correlation [58], equations (20)–(22).

$$\dot{Q}_{loss,total}(W) = \dot{Q}_{loss,rad}(W) + \dot{Q}_{loss,conv}(W) \tag{18}$$

$$\dot{Q}_{loss,rad}(W) = \sum_i A_i \cdot J_i^s + A_i \cdot J_i^r \tag{19}$$

$$\dot{Q}_{loss,conv}(W) = \sum_i A_i \cdot \dot{q}_{conv,i} = \sum_i A_i \cdot h_{conv,i} \cdot (T_i - T_{amb}) \tag{20}$$

$$Nu_i = \frac{h_{conv,i} \cdot L_{c,i}}{k_f} = 0.082 \cdot Ra^{1/3} \cdot \left[-0.9 + 2.4 \cdot \frac{T_i}{T_{amb}} - 0.5 \cdot \left(\frac{T_i}{T_{amb}} \right)^2 \right] \cdot z(Z_{w,i}) \tag{21}$$

In the above equations, $\dot{Q}_{loss,total}$ (W) is the total heat loss from the receiver; $\dot{Q}_{loss,rad}$(W) is the radiation heat loss, and $\dot{Q}_{loss,conv}$ (W) is the convection heat loss; A (m^2) is area of each surface; h_{conv} (W/m^2 − °C) is the convection heat transfer coefficient, calculated by equation (21); Ra is the Rayleigh number, T_{amb} (K) is the ambient temperature and $z(Z_{w,i})$ is the surface orientation, where $Z_{w,i}$ is the angle between the z-axis and the normal vector to the surface. The surface orientation is calculated according to equation (22).

$$z(Z_{w,i}) = \begin{cases} 1 & if \quad 0 < Z_{w,i} < 135 \ \ degrees \\ \frac{2}{3} \cdot \left[1 + \frac{sin(Z_{w,i})}{\sqrt{2}} \right] & if \quad Z_{w,i} > 135 \ \ degrees \\ \frac{2}{3} \ \ downward \ \ facing \ \ heated \ \ surface \end{cases} \tag{22}$$

The thermal efficiency of the receiver is calculated by equation (23).

$$\eta_{th} = \frac{\dot{Q}_{useful}}{\dot{Q}_{incident}} = \frac{\dot{Q}_{useful}}{\dot{Q}_{useful} + \dot{Q}_{loss,total}} \tag{23}$$

For each receiver configuration, it is necessary to calculate the optical efficiency of the associated heliostat field. For this, the program SolarPILOT is used [60]. SolarPILOT is a tool that employs both an analytical flux image Hermite series approximation (based on DELSOL [61]) and a Monte-Carlo ray tracing engine (based on SolTrace [62]). For all the layouts, it has been carried out a parametric study to calculate the tower height and the heliostat field associated, to provide the required thermal power in the receiver. The tower height values obtained are within the range of those recommended for north-facing fields [51]. Besides, SolarPILOT has been integrated into SAM software [63], so it also provides an economic assessment of the solar field investment, including the tower and receiver.

2.6. Economic model

The investment cost (fixed capital investment, FCI, according with [64]) has been estimated. This cost include both the direct and indirect costs, taken the latter as 25% of the former [64], except for the tower, receiver and solar field, as it will be discussed later. Direct costs are divided into on-site costs (ONSC: purchased-equipment costs, installation, piping, instrumentation, controls and electrical equipment) and off-site costs (OFFSC: land, civil works and service facilities). Except when a especial scale law is presented, equation (24) is used to scale the cost, where C_O stands for the base cost, C the actual cost, M_O the base magnitude, M the actual magnitude and a the escalation factor.

$$C = C_0 \cdot \left(\frac{M}{M_0} \right)^a \tag{24}$$

For the estimation of the power cycle, a study of Sandia National Laboratory [65] for a recompression cycle of 10 MWe has been taken as basis. This study allows to convert the purchased-equipment costs

(PEC) into on-site costs multiplying by 2.19. The PEC for the main equipment is scaled as follows:

(a) PCHEs. The PCHEs are scaled using the number of modules due to a module is the manufacturing unit. The escalation factor is 0.4 [64], the base PEC is 5 M$ with a number of modules of 4.46 for the HTR, and 3 M$ and 3.1, respectively, for the rest of PCHEs. The reason is that the HTR operates at temperatures which demands the use of Inconel 617 alloy, whereas the other heat exchangers are manufactured in SS 316 [30].
(b) Air cooled heat exchangers. Base cost is taken as 836,500 $, for high pressure, in SS 316, heat exchanger of inner area (bare tube) of 1000 m^2 with an escalation factor of 0.526, according with estimation of the engineering company Matches [66].
(c) Turbomachinery and generator. The escalation for the set of main compressor, auxiliary compressor, turbine and generator has been taken from [67] and is based on the three factors given in equations (25)–(27). Finally, the PEC is given by equation (28).

$$f_W = \left(\frac{W}{10MW} \right)^{0.68} \tag{25}$$

$$f_p = \left(\frac{p}{200bar} \right)^{-0.6} \tag{26}$$

$$f_T = \frac{3.35 + \left(\frac{T[\ °C]}{1000} \right)^{7.8}}{3.35 + \left(\frac{650°C}{1000} \right)^{7.8}} \tag{27}$$

$$PEC_{TMG} = f_W \cdot f_p \cdot f_T \cdot 6M\$ \tag{28}$$

As shown in equation (26), the pressure factor f_p decreases when the turbine inlet pressure is greater than 200 bar, which will lead to an investment for turbomachines lower in the proposed layout than in the conventional one.

Regarding the shell and tube heat exchangers, the PEC has been estimated using the Purohit method [68] that precisely covers this type of heat exchanger and that requires the knowledge of the characteristics, design and operating parameters of the HX. The PEC of the HX is obtained based on the cost estimated for a baseline heat exchanger and corrected by factors that consider different materials, pressures and other features. The cost, C_E ($), is estimated by equation (29), supported by equation (30), where C_b is the cost of the baseline heat exchanger fabricated from base material (carbon steel) ($/ft^2), designed to operate at a given pressure range and for a specific design type (a specific TEMA type, dimensions and geometry). D_{Sh} is the shell inside diameter (in), p is a cost multiplier for the tube outside diameter, pitch and layout angle, f is a cost multiplier for TEMA-type front head, and r is a cost multiplier for TEMA type rear head; C_i are the factors that correct the base cost due to the differences from the reference heat exchanger [68], see Table 7, and A is the heat transfer area (ft^2). The cost obtained with equation (30) is referred to 1982, so for the cost

Table 7
Corrections factors (C_i) in Purohit method for shell and tubes heat exchangers.

|	
C_S	TEMA shell type (zero if type is E, J or X)
C_X	Expansion joint
C_L	Tube length (zero if length is greater than 20 ft [6.1 m])
C_{NTP}	Tube passes (zero for one or two passes)
C_{PS}	Shellside design pressure (zero if pressure is lower than 150 psi [10.5 bar])
C_{PT}	Tubeside design pressure (zero if pressure is lower than 150 psi [10.5 bar])
C_{mt}	Tube material (zero if welded carbon steel tubes are used)
C_{ms}	Shell material (zero if carbon steel is used)
C_{mch}	Channel material (zero if carbon steel is used)
C_{mts}	Tubesheet material (zero if carbon steel is used)
C_g	Tube gage (zero for 14 BWG)
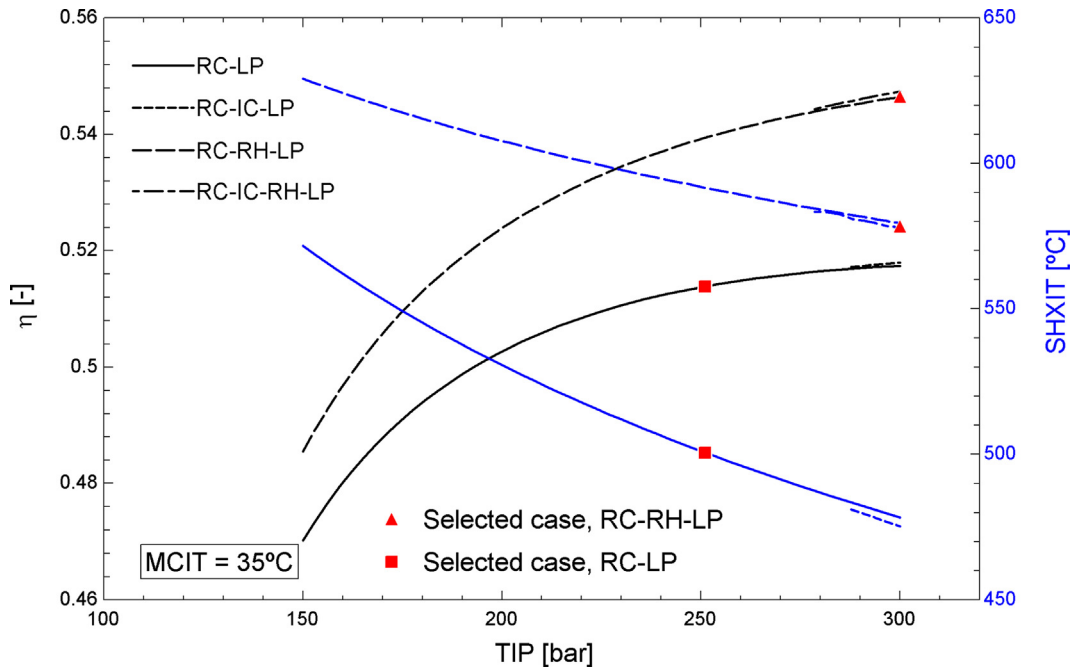
Fig. 8. Performances of different layouts when wet cooling is used.
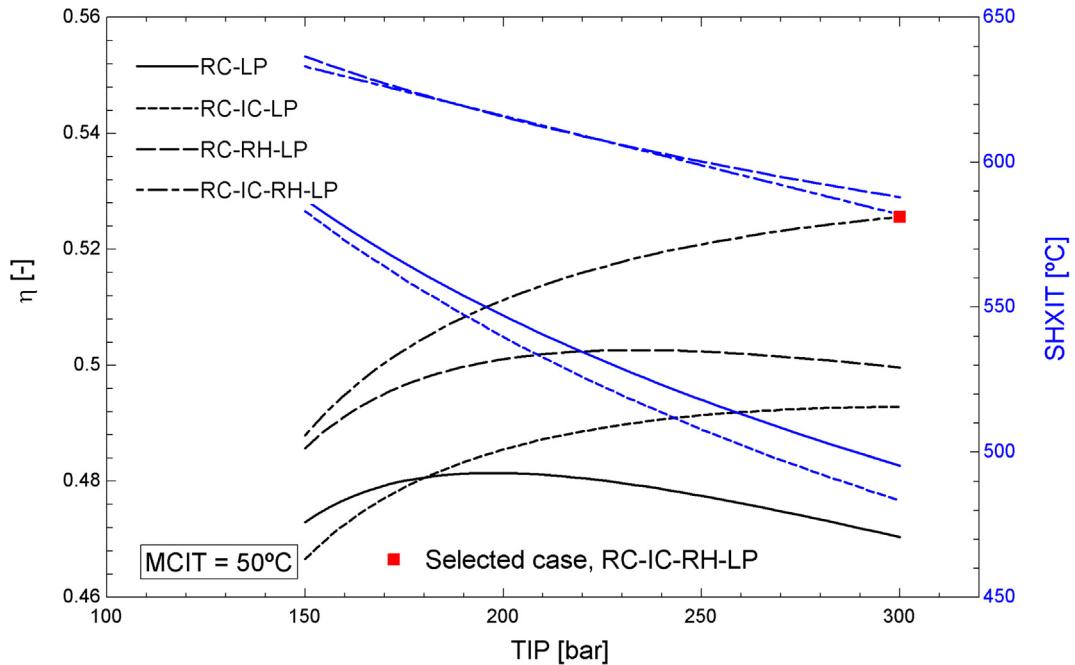

Fig. 9. Performances of different layouts when dry cooling is used.

based on different times, an escalation index is applied according with equation (31) where C_{ERy} is the estimated cost at the reference year ($), C_E is the estimated cost at the original year ($) calculated with equation (29), and CI_{Ry}/CI_{Oy} is the ratio of the cost index on the two dates [69]. The index used is the Fabricated Equipment component of the Chemical Engineering Plant Cost Index (CEPCI) (reported monthly).

$$C_E = C_b \cdot \left(1 + \sum_i C_i\right) \cdot A \tag{29}$$

$$C_b = \left[\frac{6.6}{1 - e^{((7 - D_{Sh})/27)}}\right] \cdot p \cdot f \cdot r \tag{30}$$

$$C_{ERy} = C_E \cdot \frac{CI_{Ry}}{CI_{Oy}} \tag{31}$$

Cost estimation of the thermal energy storage (TES) system has been taken from the NREL Gen3 roadmap for CSP [1], where the TES using $MgCl_2$ based salt, for 720 °C, is taken as base case. The costs are given as direct costs, so including both on-site and off-site values. The volume of the cold tank is taken as base value (30,000 m^3), being the escalation factor 0.8. The base cost for the cold tank is 16.794 M$, for the hot tank 110.119 M$, for structural steel 1.117 M$, for tank insulation 6.6243 M$, for electrical installations 1.161 M$, for foundations 5.113 M$ and for site works 0.581 M$. The salt inventory cost varies linearly with a specific cost of 295 $/tonne.
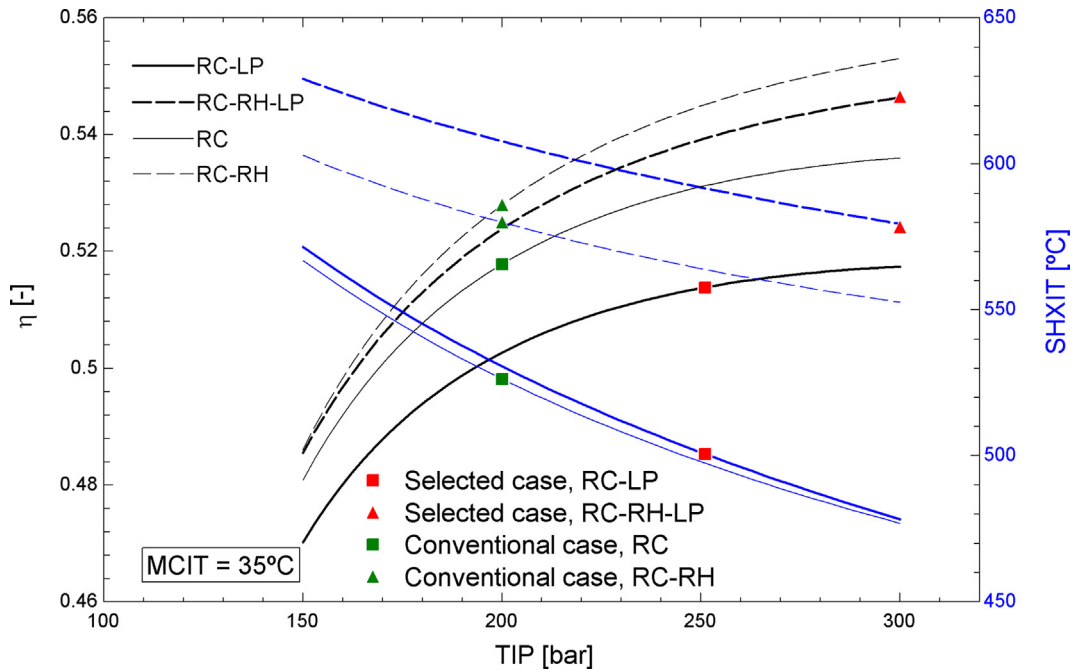
Fig. 10. Performance comparison between selected layouts of the novel cycle and the conventional layouts when wet cooling is used.
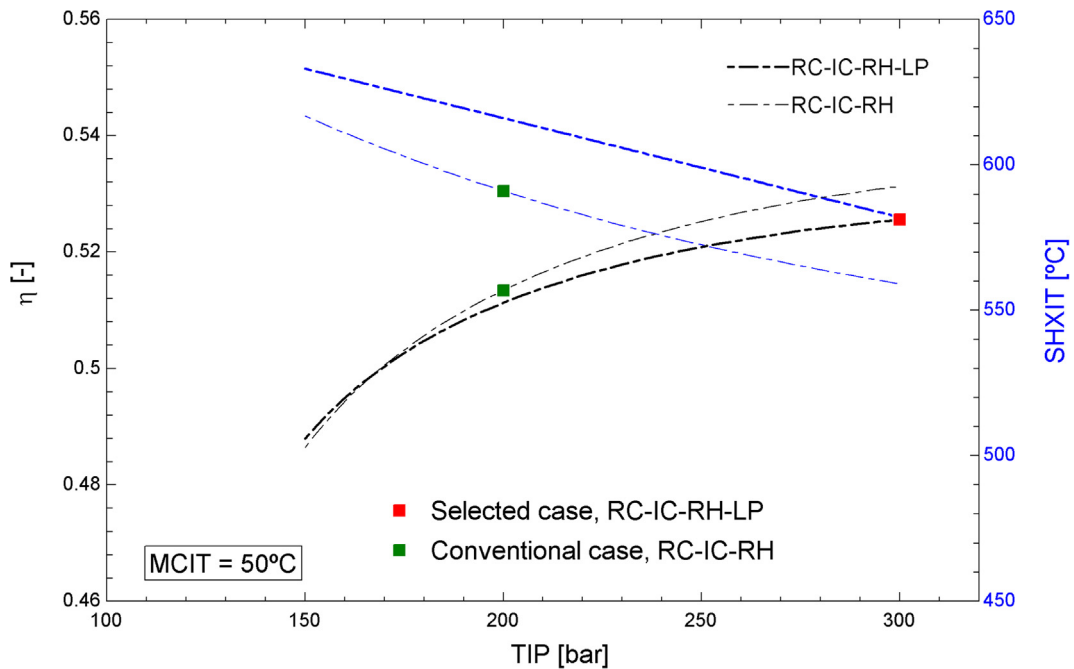
Fig. 11. Performance comparison between selected layouts of the novel cycle and the conventional layouts when dry cooling is used.

The cost of the tower, receiver and heliostat field has been estimated by means of the SolarPILOT software [70]. The on-site cost of the tower is scaled according to equation (32), as a function of the tower height (h_t). The on-site cost of the receiver is scaled with a base cost of 103 M$, a base area of 1571 m^2 and an escalation factor of 0.7. Finally, the on-site heliostat field is scaled linearly with a specific cost of 145 $/m^2 for the heliostat reflective area. Off-site costs are estimated according with 16 $/m^2 for site improvements and 24,710 $/ha for land cost. Specific ratios for contingencies and other indirect costs are implemented in the software.

$$ONSC_{tower} [M\$] = 3 \cdot e^{0.0113 \cdot h_t [m]} \tag{32}$$

3. Results

3.1. Layout selection

Two scenarios have been considered, depending on the heat sink: wet cooling and dry cooling. In the former the main compressor inlet temperature (MCIT) is assumed to be 35 °C, whereas in the latter 50 °C. In each scenario, four layouts have been tested: recompression (RC-LP), recompression with intercooling (RC-IC-LP), recompression with reheating (RC-RH-LP), and finally recompression with intercooling and reheating (RC-IC-RH-LP). When intercooling and/or reheating are used, the intermediate pressure is optimised to maximise the cycle efficiency. In all cases, the split ratio in the compressors is evaluated to obtain a

J.I. Linares, et al.   Applied Energy 263 (2020) 114644
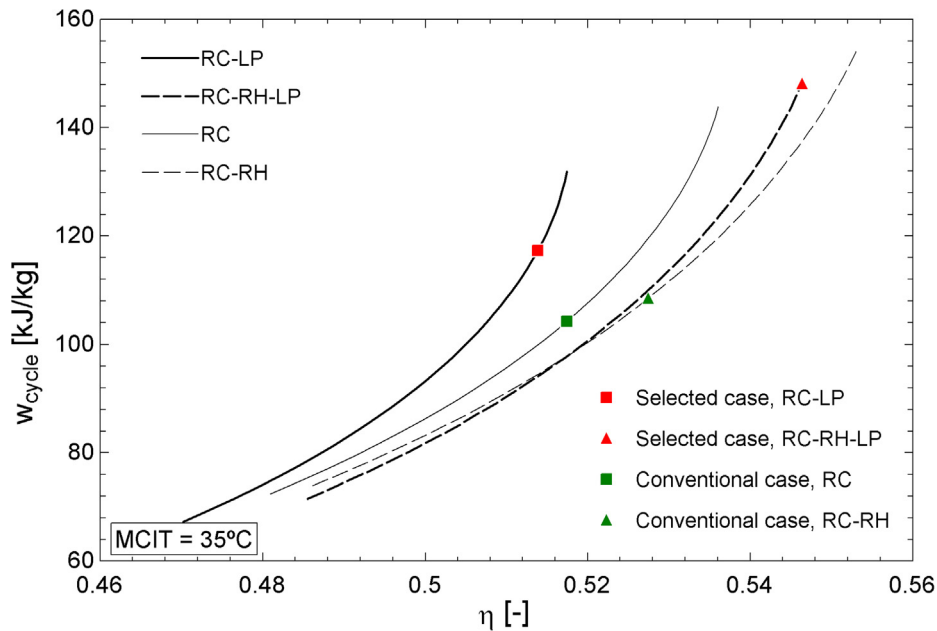

Fig. 12. Specific cycle power versus cycle efficiency for selected layouts of the novel cycle and the conventional layouts when wet cooling is used.
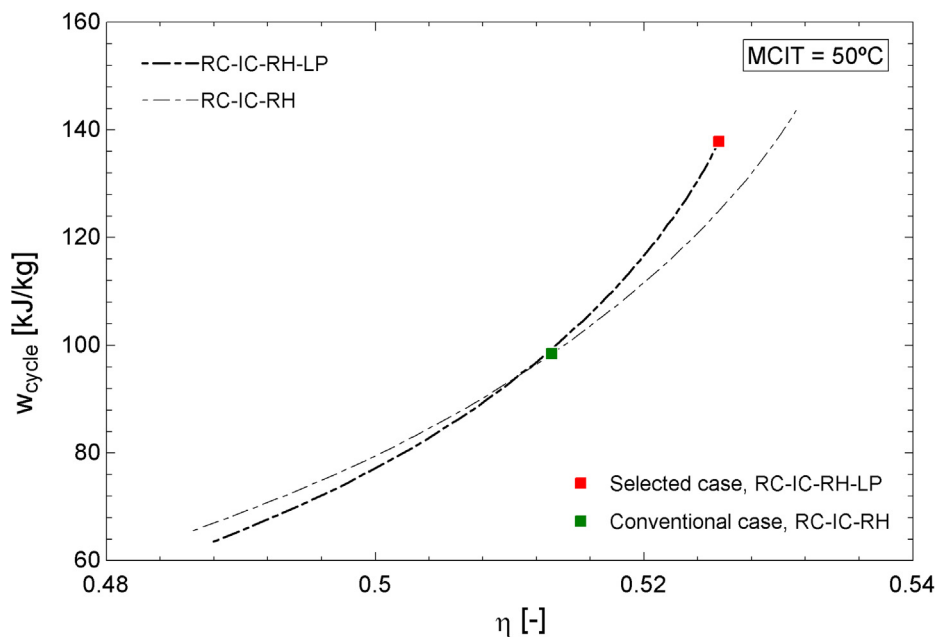

Fig. 13. Specific cycle power versus cycle efficiency between selected layouts of the novel cycle and the conventional layouts when dry cooling is used.

balanced LTR. Figs. 8 and 9 show the performance of all layouts in both cooling scenarios, as a function of the turbine inlet pressure (TIP). The cycle efficiency (η) and the CO_2 inlet temperature to the source heat exchanger (SHXIT) are obtained. This temperature is an indicator of the minimum molten salt temperature, which influences the molten salt inventory, being the maximum temperature given (700 °C).

As the main compressor inlet is close to the critical temperature when wet cooling is used, Fig. 8 shows no improvement is found if intercooling is done (using or not using reheating). In fact, only the cases with intercooling pressure higher than 90 bar have been plotted. The situation is clearly different when dry cooling is used, achieving higher efficiencies when intercooling is used, independently of reheating, which is in accordance with the findings in [19] (considering only intercooling) and [26] (several arrangements). In both cooling scenarios the SHXIT increases around 100 °C when reheating is used,

independently of intercooling, as in [18]. This will lead to a higher cost in TES when reheating is used. Trying to achieve an efficiency higher than 50%, three cases have been selected, marked with red symbols in Figs. 8 and 9. So, when wet cooling is used two configurations have been highlighted: RC-LP at 250 bar and RC-RH-LP at 300 bar. The pressure has been chosen taken into account the sensitivity of the efficiency to the turbine inlet pressure. When dry cooling is used, only the most complex layout (RC-IC-RH-LP) achieves efficiencies well above 50%. Thus, 300 bar is selected for this scenario.

In order to compare the proposed layouts with the conventional ones, Figs. 10 (wet cooling) and 11 (dry cooling) have been obtained, where the selected cases for the proposed layouts have been highlighted. In the conventional layouts the point selected for the comparison is the one at 200 bar, the maximum pressure allowed. In wet cooling cases (Fig. 10) the cycle efficiency of the simple recompression
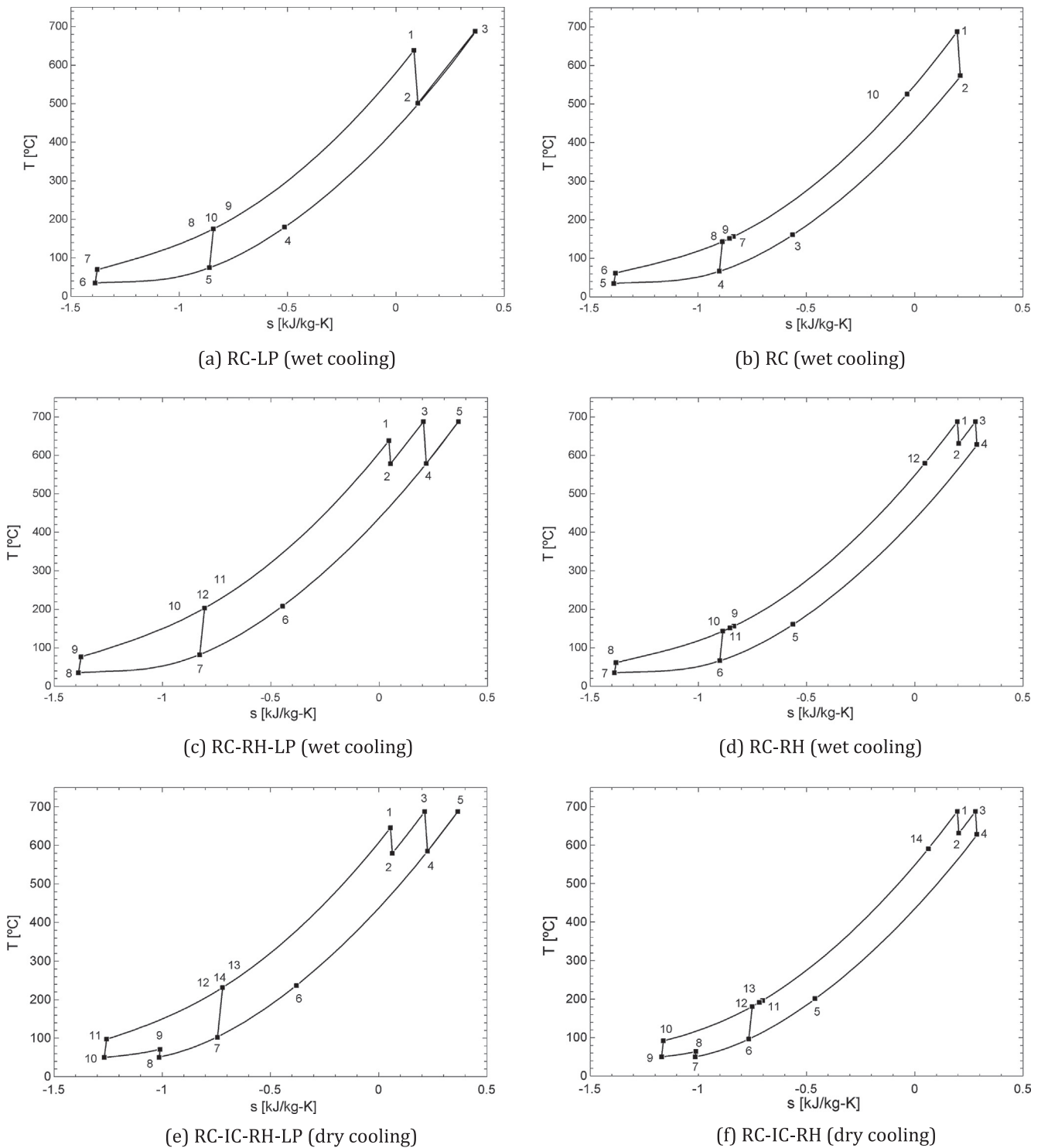
(a) RC-LP (wet cooling)

(b) RC (wet cooling)

(c) RC-RH-LP (wet cooling)

(d) RC-RH (wet cooling)

(e) RC-IC-RH-LP (dry cooling)

(f) RC-IC-RH (dry cooling)

Fig. 14. T-s diagrams of selected layouts (a, c and e) and equivalent layouts in conventional arrangements (b, d and f).

layout is slightly lower in the proposed cycle (51.37%) than in the conventional cycle (51.78%). The SHXIT is more than 25 °C lower in the proposed cycle (which implies a lower inventory of molten salt). On the contrary, for the recompression with reheating layout, a larger efficiency in the proposed cycle is achieved (54.64% versus 52.79%), but similar SHXIT. Similarly, in the dry cooling case, the cycle efficiency of the recompression with intercooling and reheating layout is higher in the proposed cycle (52.56% versus 51.34%), with similar values of SHXIT. Thus, the higher efficiencies achieved in the proposed cycles are not meaningful (3.5% in the best case). The increase in the pressure

values are compensated by the reduction in the turbine inlet temperatures (in fact, in the basic recompression layout, the conventional cycle reaches a higher efficiency than in the proposed cycle). In conclusion, the results obtained indicate that the proposed layout gives an efficiency similar to the achieved with the conventional one.

However, the most important feature of the proposed cycle is the higher compactness, which is derived from Figs. 12 (wet cooling) and 13 (dry cooling). These figures show the specific cycle power versus the cycle efficiency classic diagram [10] updated for S-CO$_2$, where each point corresponds with a turbine inlet pressure. These figures show an

Table 8
State points of the selected layouts in the proposed cycles.

	RC-LP (wet cooling)			RC-RH-LP (wet cooling)			RC-IC-RH-LP (dry cooling)		
	p [bar]	T [°C]	h [kJ/kg]	p [bar]	T [°C]	h [kJ/kg]	p [bar]	T [°C]	h [kJ/kg]
1	250	638.6	636.7	300	638.4	634.4	300	645.6	643.6
2	86.6	501.1	478.7	193.4	578.4	564	185.5	579.8	566.3
3	86.2	688	706.4	193	688	701.6	185.1	688	701.9
4	85.8	180.2	107.9	86.6	579.3	572.8	86.6	584.8	579.5
5	85.4	74.6	−29.27	86.2	688	706.4	86.2	688	706.4
6	85	35	−197.9	85.8	208.2	140.2	85.8	236.3	172.2
7	250.8	69.6	−170.7	85.4	81.62	−17.91	85.4	102.4	12.3
8	250.4	175.2	38.19	85	35	−197.9	85	50	−80.9
9	250.4	175.2	38.19	300.8	76.62	−163.2	111.8	71.27	−69.79
10	250.4	175.2	38.19	300.4	203.2	68.19	111.4	50	−155.6
11	–	–	–	300.4	203.2	68.19	300.8	97.43	−120.4
12	–	–	–	300.4	203.2	68.19	300.4	231.3	109.5
13	–	–	–	–	–	–	300.4	231.3	109.5
14	–	–	–	–	–	–	300.4	231.3	109.5

Table 9
State points of the conventional cycles.

	RC (wet cooling)			RC-RH (wet cooling)			RC-IC-RH (dry cooling)		
	p [bar]	T [°C]	h [kJ/kg]	p [bar]	T [°C]	h [kJ/kg]	p [bar]	T [°C]	h [kJ/kg]
1	200	688	701.3	200	688	701.3	200	688	701.3
2	86.2	574.1	566.5	133.1	631.1	633.2	133.1	631.1	633.2
3	85.8	161.5	85.94	132.7	688	704.1	132.7	688	704.1
4	85.4	66.69	−43.29	86.2	628.6	633	86.2	628.6	633
5	85	35	−197.9	85.8	161.5	85.94	85.8	201.5	132.5
6	201.2	61.69	−178.4	85.4	66.69	−43.29	85.4	96.42	3.972
7	200.8	156.5	26.51	85	35	−197.9	85	50	−80.9
8	200.8	143.2	4.687	201.2	61.69	−178.4	101.4	63.65	−73.85
9	200.8	151.5	18.45	200.8	156.5	26.51	101	50	−126.1
10	200.4	526.3	499	200.8	143.2	4.687	201.2	91.42	−102
11	–	–	–	200.8	151.5	18.45	200.8	196.5	85.84
12	–	–	–	200.4	579.9	565.5	200.8	180.9	63.57
13	–	–	–	–	–	–	200.8	191.5	78.81
14	–	–	–	–	–	–	200.4	591	579.3

Table 10
Performances of the selected layouts (in the case of dry cooling, CP stands for the consumption of the fans).

	Wet cooling		Dry cooling
	RC-LP	RC-RH-LP	RC-IC-RH-LP
MC1 [MW]	7.65	8.00	2.80
MC2 [MW]	–	–	8.87
AC [MW]	9.91	9.2	10.72
HPT [MW]	67.53	23.76	28.04
LPT [MW[	–	43.44	44.36
SHX [MW]	97.33	45.09	45.99
RH [MW]	–	46.42	49.14
PC [MW]	47.33	41.52	23.50
IC [MW]	–	–	21.64
HTP [MW]	0.18	0.22	0.32
LTP [MW]	0.26	0.32	0.47
CP [MW]	0.76	0.67	0.1
$\dot{W}_{cycle}$ [MW]	50.00	50.00	50.00
$\dot{W}_{gross}$ [MW]	48.5	48.5	48.5
$\dot{W}_{net}$ charge period [MW]	47.30	47.29	47.61
$\dot{W}_{net}$ discharge period [MW]	47.56	47.61	48.08
Cycle efficiency [%]	51.37	54.64	52.56

important increment of the specific cycle efficiency in the proposed cycles, as expected. So, in wet cooling the specific work rises from 104.8 kJ/kg in RC to 117 kJ/kg in RC-LP (11.2% of relative increment) and from 109.1 kJ/kg in RC-RH to 148.1 kJ/kg in RC-RH-LP (35.7% of relative increment). In dry cooling the trend is the same: from 98.99 kJ/

kg in RC-IC-RH to 138 kJ/kg in RC-IC-RH-LP (39.4% of relative increment). These increases in the specific cycle work are translated into decreases in the mass flow rate in the novel cycle, so leading to a higher compactness, lower investments and a better dynamic response.

3.2. Analysis of selected layouts

Fig. 14 shows the T-s diagram for conventional and proposed cycles. The low pressure heating supply can be observed in the 2–3 process in Fig. 14a, and in the 4–5 process in Fig. 14c and e. In the case of reheating, the intermediate pressure is low enough to allow the use of a STHX, although with tubes of large thickness. It can be seen the larger areas enclosed by the cycles in the proposed arrangements compared with the conventional cases, as previously mentioned, which produces a larger specific cycle work. Table 8 gives the state points for the proposed cycles and Table 9 for the conventional ones. They are referred to the different label points shown in Fig. 3, and have been obtained from the cycle models described in Section 2.2.

Once it has been checked that the proposed cycle achieves similar efficiencies and a higher compactness than the conventional one, the sizing and investment assessment have been carried out for the selected layouts of the proposed cycle. So, taken into account the model and assumption given in Sections 2.2 and 2.5.1, the performance of the selected cycles is summarised in Table 10. This table shows a consumption power in the cooling loop between 670 kW and 760 kW in wet cooling and 100 kW in dry cooling. This lower consumption in the dry cooling compensates the reduction in the cycle efficiency. The effectiveness of this design criterion can be checked in the net power

Table 11
Main dimensions of PCHEs.

			LTR	HTR	PC
Wet cooling	RC-LP	Heat power [MW]	58.62	255.84	47.33
		Height [m]	3.90	2.66	0.66
		Length [m]	10.74	12.64	3.12
		Width [m]	0.60	0.60	0.60
		Volume [m^3]	25.11	20.17	1.25
		Number of modules (actual)	53.70	42.12	5.21
		Number of modules (base)	3.1	4.46	3.1
		Base PEC [M$]	3.0	5.0	3.0
		Actual PEC [M$]	9.4	12.3	3.7
	RC-RH-LP	Heat power [MW]	53.36	191.13	41.52
		Height [m]	4.39	2.62	0.66
		Length [m]	9.36	10.02	2.75
		Width [m]	0.60	0.60	0.60
		Volume [m^3]	24.64	15.72	1.09
		Number of modules (actual)	46.80	33.4	4.59
		Number of modules (base)	3.1	4.46	3.1
		Base PEC [M$]	3.0	5.0	3.0
		Actual PEC [M$]	8.9	11.2	3.5
Dry cooling	RC-IC-RH-LP	Heat power [MW]	57.97	193.59	–
		Height [m]	3.37	2.82	–
		Length [m]	9.35	11.45	–
		Width [m]	0.60	0.60	–
		Volume [m^3]	18.91	19.36	–
		Number of modules (actual)	46.74	38.16	–
		Number of modules (base)	3.1	4.46	–
		Base PEC [M$]	3.0	5.0	–
		Actual PEC [M$]	8.9	11.8	–

Table 12
Main dimensions of air cooled heat exchangers.

			PC	IC
Dry cooling	RC-IC-RH-LP	Heat power [MW]	23.50	21.64
		Tube length [m]	18.2	29.75
		Air length [m]	0.17	0.23
		Frontal area [m^2]	475	510
		Volume [m^3]	78.97	118.1
		Heat transfer inner area (actual) [m^2]	3943	5899
		Heat transfer inner area (base) [m^2]	1000	1000
		Base PEC [M$]	0.837	0.837
		Actual PEC [M$]	1.72	2.13

Table 13
Main dimensions of STHXs.

			SHX	RH
Wet cooling	RC-LP	Number of units	2	–
		Heat power [MW]	48.665	–
		Tube outer diameter [mm]	15.875	–
		Tube thickness [mm]	2.768	–
		Tube pitch [mm]	19.843	–
		Number of tube passes	1	–
		Number of shell passes	1	–
		Heat transfer area [m^2]	17,085	–
		Length [m]	28.36	–
		Shell diameter [m]	2.6	–
	RC-RH-LP	Number of units	1	2
		Heat power [MW]	45.09	23.21
		Tube outer diameter [mm]	19.05	19.05
		Tube thickness [mm]	3.404	5.3
		Tube pitch [mm]	23.81	23.81
		Number of tube passes	1	1
		Number of shell passes	1	1
		Heat transfer area [m^2]	12,786	7349
		Length [m]	20.43	15.21
		Shell diameter [m]	2.9	2.55
Dry cooling	RC-IC-RH-LP	Number of units	1	2
		Heat power [MW]	45.94	24.57
		Tube outer diameter [mm]	19.05	19.05
		Tube thickness [mm]	3.40	5.3
		Tube pitch [mm]	23.81	23.81
		Number of tube passes	1	1
		Number of shell passes	1	1
		Heat transfer area [m^2]	10,320	8426
		Length [m]	16.72	15.59
		Shell diameter [m]	2.88	2.69

produced, very similar in the three cases analysed.

Based on Section 2.4 the size of the different heat exchangers is obtained, summarising the main dimensions in Table 11 for the PCHEs and Table 12 for the air cooled heat exchangers. In these tables the basis costs and the scaled investments (Section 2.6) have been also included, along with the PEC obtained. Table 13 gives the main dimensions of the STHXs, and Table 14 the breakdown of the different coefficients to determine the PEC (Section 2.6). The main characteristics of the thermal storage, taking into account the assumptions detailed in Section 2.5.1, are shown in Table 15. Finally, the main features of the receiver and the heliostat field, with the considerations explained in Section 2.5.2, are summarised in Tables 16 and 17, respectively.

3.3. Investment estimation

Economic model description given in Section 2.6 is applied to obtain all the results given in this section. Tables 18 and 19 summarise the investments in the wet cooling scenario and Table 20 in the dry cooling. The fixed capital investment in wet cooling scenario ranges from 434.6 M$ for the recompression layout to 433.1 M$ for the recompression with reheating; in dry cooling the fixed capital investment

is 437.1 M$. These values lead to 8691 $/kWe in recompression and 8662 $/kWe in recompression with reheating, both in wet cooling scenario, and 8742 $/kWe in dry cooling scenario. Projections of the Gen3 Roadmap [1] establish 200 M$ for a prototype of 10 MWe. Thus, scaling to 50 MWe, it would become into 579 M$. In such projections, a TES of 1350 MWh-th for 50 MWe is considered, with a cost (direct plus indirect costs) of 112.6 M$. Subtracting this cost to the projected investment and adding the cost of the TES in the proposed layouts (from 32.6 to 52.1 M$, considering both direct and indirect costs) results in a range for the investment between 499.0 and 518.5 M$. So, the proposed layout reduces the projections of Gen3 Roadmap between 12.9 and 15.7%. Taking into account the uncertainties in the economic model, it could be more appropriate to say that the proposed layout investment is in accordance with the Gen3 Roadmap forecasts.

Table 20 reveals the reduced importance of the investment of the air cooled heat exchangers, lower than 3% of the overall investment in the heat exchangers. This means that the selected power consumption in the fans (50 kW), which entails to large heat exchangers, is not meaningful in the final investment, contributing to control the pumping losses, as previously explained.

Fig. 15 shows an investment breakdown of the selected options into the main components. The heat exchanger contributions round 50%, being followed by the solar field, tower and receiver, which accumulate 30%. The turbomachines contribution is similar in all the cases (10%), ranging the storage system share from 8% in RC-LP wet cooling to 11% for both reheating cases. The cost increase of the storage system is due to the molten salt cold temperature reduction in the reheated layouts (80 °C in RC-RH-LP and 85 °C in RC-IC-RH-LP regarding to RC-LP), which leads to an increase of 62% and 77% in the salt inventory in wet and dry reheating layouts, respectively.

Although the investment assessment of the conventional layout has not been carried out, the investment for shell and tubes heat exchangers in RC-IC-RH-LP can be used to estimate the general trend. So, the PEC in SHX (85 bar; 45.94 MW) is 19.7 M$, whereas the PEC in RH (185.5 bar; 49.14 MW) is 35.7 M$ (81% higher than SHX for similar

Table 17
Main characteristics of heliostat field.

	Wet cooling		Dry cooling
	RC-LP	RC-RH-LP	RC-IC-RH-LP
Simulated heliostat area [m²]	488,276	488,276	488,276
Simulated heliostat count	3382	3382	3382
Optimized tower optical height [m]	150	150	150
Cloudiness efficiency [%] min/mean/max	100/100/100	100/100/100	100/100/100
Shading efficiency [%] min/mean/max	100/100/100	100/100/100	100/100/100
Cosine efficiency [%] min/mean/max	59.02/86.45/99.98	59.02/86.45/99.98	59.02/86.45/99.98
Reflection efficiency [%] min/mean/max	90.25/90.25/90.25	90.25/90.25/90.25	90.25/90.25/90.25
Blocking efficiency [%] min/mean/max	53.11/97.23/100	53.11/97.23/100	53.11/97.23/100
Attenuation efficiency [%] min/mean/max	87.1/91.75/97.42	87.1/91.75/97.42	87.1/91.75/97.42
Image intercept efficiency [%] min/mean/max	0.2/58.81/96.78	0.19/57.93/95.64	0.2/59.08/97.14
Solar field optical efficiency [%] min/mean/max	0.09/42.23/84.3	0.09/41.63/83.93	0.1/42.41/84.4

Table 18
Summary of investments in RC-LP (wet cooling scenario).

	PEC [M$]	Direct costs [M$]		Indirect costs [M$]
		ONSC [M$]	OFFSC [M$]	
Turbomachinery	15.8	34.4	–	61.2
PCHEs				
LTR	9.4	20.5	–	
HTR	12.3	26.8	–	
PC	3.7	8.0	–	
Air Cooled heat exchangers				
PC	–	–	–	
IC	–	–	–	
STHXs				
SHX (two units; total cost)	59.3	129.2	–	
RH	–	–	–	
TES	–	26.1		
Tower	–	16.34	–	15.0
Receiver	–	18.82	–	
Solar Field	–	70.80	–	
Lands, site improvements	–	–	7.42	
Fixed capital investment [M$]		434.6		

Table 19
Summary of investments in RC-RH-LP (wet cooling scenario).

	PEC [M$]	Direct costs [M$]		Indirect costs [M$]
		ONSC [M$]	OFFSC [M$]	
Turbomachinery	14.1	30.8	–	61.1
PCHEs				
LTR	8.9	19.4	–	
HTR	11.2	24.4	–	
PC	3.5	7.6	–	
Air Cooled heat exchangers				
PC	–	–	–	
IC	–	–	–	
STHXs				
SHX	25.9	56.4	–	
RH (two units; total cost)	30.7	66.9	–	
TES	–	38.9		
Tower	–	16.3	–	15.0
Receiver	–	18.2	–	
Solar Field	–	70.8	–	
Lands, site improvements	–	–	7.4	
Fixed capital investment [M$]		433.1		

Table 20
Summary of investments in RC-IC-RH-LP (dry cooling scenario).

	PEC [M$]	Direct costs [M$]		Indirect costs [M$]
		ONSC [M$]	OFFSC [M$]	
Turbomachinery	14.1	30.8	–	61.7
PCHEs				
LTR	8.9	19.4	–	
HTR	11.8	25.7	–	
PC	–	–	–	
Air Cooled heat exchangers				
PC	1.72	3.75	–	
IC	2.13	4.64	–	
STHXs				
SHX	19.7	43.0	–	
RH (2two units; total cost)	35.7	77.9	–	
TES	–	41.7		
Tower	–	16.3	–	15.0
Receiver	–	19.0	–	
Solar Field	–	70.8	–	
Lands, site improvements	–	–	7.43	
Fixed capital investment [M$]		437.1		

have been carried out.

Two scenarios have been investigated: dry cooling and wet cooling. In the former, the highest efficiency is achieved in the recompression with intercooling and reheating layout, reaching a value of 52.6% at 300 bar of turbine inlet pressure. Options without reheating (with or without intercooling) have been discarded because they do not reach 50%, while reheating with intercooling does at 225 bar. In the wet cooling scenario, the recompression cycle (neither intercooled not reheated) exceeds 51% efficiency at 250 bar, increasing to more than 54% if reheating is added. The efficiency does not take advantage of intercooling in the wet scenario. If 50% cycle efficiency is set as a goal for advanced solar plants, recompression in wet cooling scenario might be the first prototype to test in this new technology, loosing 0.4 percentage points regarding the conventional supercritical CO_2 Brayton cycle (which is limited to 200 bar of turbine inlet pressure to use shell and tube heat exchangers). The inclusion of reheating always reduces the molten salt temperature gap, so increasing the salt inventory (roughly 62% in wet scenario). Regarding the economic assessment, all the analysed layouts range between 8614 to 8742 $/kWe for a plant of 50 MWe, in accordance with the projections of Gen3 Roadmap.

The proposed cycle takes advantage of the higher turbine inlet pressure to increase the specific cycle work, compensating the lower turbine inlet temperature with the higher pressure. Moreover, the reduction in the working pressure of the shell and tubes heat exchangers allows to decrease significantly the investment of the heat exchangers. So, the proposed cycle is able to face the potential salt clogging/thawing issues, achieving a higher compactness (better dynamic response) and lower investments, maintaining the efficiency.

CRediT authorship contribution statement

José I. Linares: Conceptualization, Methodology, Investigation, Software, Writing - original draft, Supervision. **María J. Montes:** Methodology, Investigation, Software, Investigation, Writing - original draft, Project administration, Funding acquisition. **Alexis Cantizano:** Methodology, Software, Validation, Resources, Writing - review & editing. **Consuelo Sánchez:** Methodology, Software, Validation, Resources, Writing - review & editing.
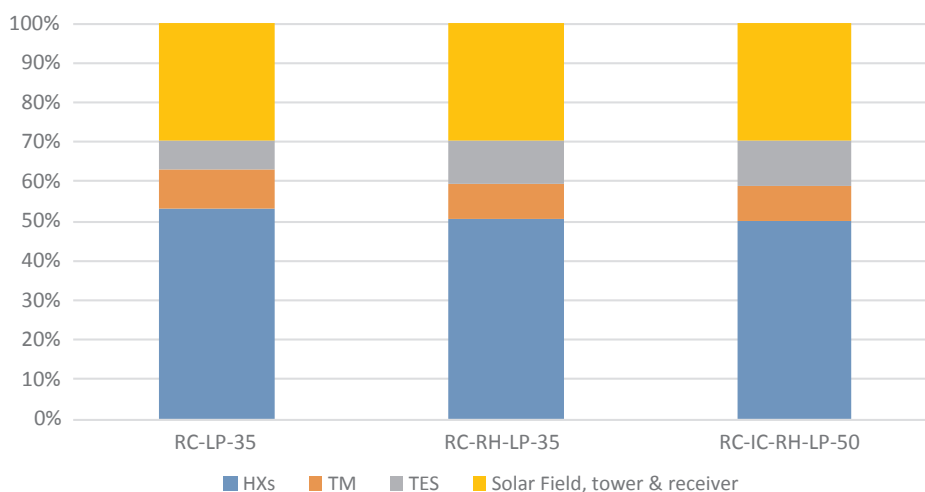
Fig. 15. Investment (fixed capital investment) breakdown of the selected options.

Declaration of Competing Interest

References

[1] Mehos M, Turchi C, Vidal J, Wagner M, Ma Z, Ho C, et al. Concentrating Solar Power Gen3 Demonstration Roadmap. NREL, NREL/TP-5500-67464; 2017.

[2] Gurgenci H, Stein W, Beath A, Blanco M, Sauret E. The case for supercritical CO_2 radial turbine development within the Australian Solar Thermal Research nitiative (ASTRI) program. Proceedings of the 52nd annual conference. Melbourne: Australian Solar Energy Society (Australian Solar Council); 2014.

[3] Zhang J. Dynamic modelling and transient analysis of a molten salt heated re-compression supercritical CO_2 Brayton cycle. Proceedings of the 5th International Supercritical CO_2 Power Cycles Symposium, Pennsylvania, USA, March 2018. 2018.

[4] Myers PD, Goswami DY. Thermal energy storage using chloride salts and their eutectics. Appl Therm Eng 2016;109:889–900.

[5] Li Y, Xu X, Wang X, Li P, Hao Q, Xiao B. Survey and evaluation of equations for thermophysical properties of binary/ternary eutectic salts from NaCl, KCl, $MgCl_2$, $CaCl_2$ and $ZnCl_2$ for heat transfer and thermal storage fluids in CSP. Sol Energy 2017;152:57–79.

[6] Mohan G, Venkataraman M, Gomez-Vidal J, Coventry J. Assessment of a novel ternary eutectic chloride salt for next generation high-temperature sensible heat storage. Energy Convers Manage 2018;167:156–64.

[7] Xu X, Dehghani G, Ning J, Li P. Basic properties of eutectic chloride salts NaCl-KCl-$ZnCl_2$ and NaCl-KCl-$MgCl_2$ as HTFs and thermal storage media measured using simultaneous DSC-TGA. Sol Energy 2018;162:431–41.

[8] Turchi CS, Vidal J, Bauer M. Molten salt power towers operating at 600–650 °C: Salt selection and cost benefits. Sol Energy 2018;164:38–46.

[9] Ho CK, Iverson BD. Review of high-temperature central receiver designs for concentrating solar power. Renew Sustain Energy Rev 2014;29:835–46.

[10] Saravanamuttoo HIH, Rogers GFC, Cohen H, Straznicky PV, Nix AC. Gas Turbine Theory, Pearson. 7th edition, 2017.

[11] Herranz LE, Linares JI, Moratilla BY. Power cycle assessment of nuclear high temperature gas-cooled reactors. Appl Therm Eng 2009;29:1759–65.

[12] Pérez-Pichel G, Linares JI, Herranz LE, Moratilla BY. Potential application of Rankine and He-Brayton cycles to sodium fast reactors. Nucl Eng Des 2011;241:2643–52.

[13] Pérez-Pichel G, Linares JI, Herranz LE, Moratilla BY. Thermal analysis of supercritical CO_2 power cycles: assessment of their suitability to the forthcoming sodium fast reactors. Nucl Eng Des 2012;250:23–34.

[14] Sulzer G. Verfahren zur Erzeugung von Arbeit aus Warme, Swiss Patent 269599; 1950.

[15] Angelino G. Carbon dioxide condensation cycles for power production. J Eng Power 1968;90:287–95.

[16] Feher EG. The supercritical thermodynamic power cycle. Energy Convers 1968;8:85–90.

[17] Dostal V. A supercritical carbon dioxide cycle for next generation nuclear reactors [Doctoral Thesis]. Massachusetts: Institute of Technology; 2004.

[18] Wang K, He YL, Zhu HH. Integration between supercritical CO_2 Brayton cycles and molten salt solar power towers: A review and comprehensive comparison of different cycle layouts. Appl Energy 2017;195:819–36.

[19] Ma Y, Liu M, Yan J, Liu J. Thermodynamic study of main compression intercooling effects on supercritical CO_2 recompression Brayton cycle. Energy 2017;140:746–56.

[20] Binotti M, Astolfi M, Campanari S, Manzolini G, Silva P. Preliminary assessment of SOC2 cycles for power generation in CSP solar tower plants. Appl Energy 2017;204:1007–17.

[21] Iverson BD, Conboy TM, Pasch JJ, Kruizenga AM. Supercritical CO_2 Brayton cycles for solar-thermal energy. Appl Energy 2013;111:957–70.

[22] Ahn Y, Bae SJ, Kim M, Cho SK, Baik S, Lee JI, et al. Review of supercritical CO_2 power cycle technology and current status of research and development. Nucl Eng Technol 2015;47:647–61.

[23] Li M, Zhu H, Guo J, Wang K, Tao W. The development technology and applications of supercritical CO_2 power cycle in nuclear energy, solar energy and other energy industries. Appl Therm Eng 2017;126:255–75.

[24] Turchi CS, Ma Z, Neises TW, Wagner MJ. Thermodynamic study of advanced supercritical carbon dioxide power cycles for concentrating solar power systems. J Sol Energy Eng 2013;135(041007–1):041007–41017.

[25] Milani D, Luu MT, McNaughton R, Abbas A. Optimizing an advanced hybrid of solar-assisted supercritical CO_2 Brayton cycle: a vital transition for low-carbon power generation industry. Energy Convers Manage 2017;148:1317–33.

[26] Wang K, Li MJ, Guo JQ, Li P, Liu ZB. A systematic comparison of different S-CO_2 Brayton cycle layouts based on multi-objective optimization for applications in solar power tower plants. Appl Energy 2018;212:109–21.

[27] Xu J, Liu Ch, Sun E, Xie J, Li M, Yang Y, et al. Perspective of S-CO_2 power cycles. Energy 2019;186:115831.

[28] Ma Z, Turchi CS. Advanced supercritical carbon dioxide power cycle configurations for use in concentrating sola power systems. Proceedings of the 3rd Supercritical CO_2 Power Cycle Symposium, Colorado, USA, May 2011. 2011.

[29] Pierres RL, Southall D, Osborne S. Impact of mechanical design issues on printed circuit heat exchangers. Proceedings of 3rd SCO2 Power Cycle Symposium, Colorado, USA, May 2011. 2011.

[30] Southall D, Pierres RL, Dewson SJ. Design considerations for compact heat exchangers. Proceedings of ICAPP '08, California, USA, June 2008. 2008.

[31] Huang Ch, Cai W, Wang Y, Liu Y, Li Q, Li B. Review on the characteristics of flow and heat transfer in printed circuit heat exchangers. Appl Therm Eng 2019;153:190–205.

[32] Moore R, Vernon M, Ho CK, Siegel NP, Kolb GJ. Design considerations for concentrating solar power tower systems employing molten salt. Sandia Report SAND2010-6978; 2010.

[33] Sabharwall P, Clark D, Glazoff M, Zheng G, Sridharan K, Anderson M. Advanced heat exchangers development for molten salts. Nucl Eng Des 2014;280:42–56.

[34] Lao J, Ding J, Fu Q, Wang W, Lu J. Heat transfer between molten salt and supercritical CO_2 in discontinuous fins print circuit heat exchanger. Energy Procedia 2019;158:5832–7.

[35] Wang WQ, Qiu Y, He YL, Shi HY. Experimental study on the heat transfer performance of a molten-salt printed circuit heat exchanger with airfoil fins for concentrating solar power. Int J Heat Mass Transf 2019;135:837–46.

[36] Kruizenga A, Fleming D. Materials Corrosion Concerns for Supercritical Carbon Dioxide Heat Exchangers. Sandia National Laboratories, SAND2014-15095PE; 2014.

[37] He YL, Zheng ZJ, Du BC, Wang K, Qiu Y. Experimental investigations on turbulent heat transfer characteristics of molten salt in a shell-and-tube heat exchanger. Appl Therm Eng 2016;108:1206–13.

[38] Qiu Y, Li MJ, Wang WQ, Du BC, Wang K. An experimental study on the heat transfer performance of a prototype molten-salt rod baffle heat exchanger for concentrated

solar power. Energy 2018;156:63–72.

[39] Linares JI, Cantizano A, Arenas E, Moratilla BY, Martín-Palacios V, Batet Ll. Recuperated versus single-recuperator re-compressed supercritical CO_2 Brayton power cycles for DEMO fusion reactor based on dual coolant lithium lead blanket. Energy 2017;140:307–17.

[40] Moisseytsev A, Sienicki JJ. Investigation of alternative layouts for the supercritical carbon dioxide Brayton cycle for a sodium-cooled fast reactor. Nucl Eng Des 2009;239:1362–71.

[41] Bahamonde-Noriega JS. Design method for S-CO2 gas turbine power plants [MSc Dissertation]. The Netherlands: Delft University of Technology; 2012.

[42] Medrano M, Puente D, Arenaza E, Herrazti B, Paule A, Brañas B, et al. Power conversion cycles study for He-cooled reactor concepts for DEMO. Fusion Eng Des 2007;2689–95.

[43] Jonemann M, Russell H, Blair R, Raade J, Ames C. System integration of contain-erized molten salt thermal energy storage in novel cascade layout. California Energy Commission. Energy Research and Development Division. (CEC-500-2016-006); 2015.

[44] Latham H, Clarkson P. Fusion Balance of Plant Assessment (under EFDA Work Package WP12-DAS08-BoP, IDM reference No. 2LLNBX, 2013).

[45] Klein SA, Nellis GF. Mastering EES, F-Chart Software, edition 63. http://www.fchartsoftware.com/ees/mastering-ees.php.

[46] Serrano IP, Cantizano A, Linares JI, Moratilla BY. Modeling and sizing of the heat exchangers of a new supercritical CO2 Brayton power cycle for energy conversion for fusion reactors. Fusion Eng Des 2014;89:1905–8.

[47] Supercritical CO2 as heat trasnfer fluid: A review. Appl Therm Eng 2017;125:799–810.

[48] Kakaç S, Liu H, Pramuanjaroenkij A. Heat exchangers: selection, rating, and thermal design, 3rd ed. Taylor & Francis; 2012. ISBN: 978-1-4398-4990-3.

[49] Standards of the Tubular Exchanger Manufacturers Association, TEMA (Tubular Exchanger Manufacturers Association), Tarrytown, NY, 8th edition; 1999.

[50] ASME Boiling and Pressure Vessel Code; 2019.

[51] Falcone PK. A Handbook for Solar Central Receiver Design, SAND 86-8009; 1986.

[52] Zavoico AB. Solar Power Tower. Design Basis Document, Sandia Report SAND2001-2100; 2001.

[53] Liao Z, Li X, Xu C, Chang C, Wang Z. Allowable flux density on a solar central receiver. Renew Energy 2014;62:747–53.

[54] Standards of the Tubular Exchanger Manufacturers Association, TEMA (Tubular

[55] Li X, Kong W, Wang Z, Chang C, Bai F. Thermal model and thermodynamic per-formance of molten salt cavity receiver. Renew Energy 2010;35:981–8.

[56] Boudaoud S, Khellaf A, Mohammedi K, Behar O. Thermal performance prediction and sensitivity analysis for future deployment of molten salt cavity receiver solar power plants in Algeria. Energy Convers Manage 2015;89:655–64.

[57] Siegel R, Howell JR. Thermal radiation heat transfer, 3rd ed. Taylor & Francis; 1992. ISBN: 0-89116-271-2.

[58] Samanes J, García-Barberena J, Zaversky F. Modeling solar cavity receivers: a re-view and comparison of natural convection heat loss correlations. Energy Procedia 2015;69:543–52.

[59] Ho CK. Advances in central receivers for concentrating solar applications. Sol Energy 2017;152:38–56.

[60] Wagner MJ, Wendelin T. SolarPILOT: A power tower solar field layout and char-acterization tool. Sol Energy 2018;171:185–96.

[61] Kistler B. A user's Manual for DELSOL3: A Computer Code for Calculating the Optical Performance and Optimal System Design for Solar Thermal Central Receiver Plants., Sandia Report SAND86-8018; 1986.

[62] Wendelin T. SolTRACE: a new optical modeling tool for concentrating solar optics. In: ASME 2003 International Solar Energy Conference, Kohala Coast, HI; 2003.

[63] Blair N, Diorio N, Freeman J, Gilman P, Janzou S, Neises T, et al. System Advisor Model (SAM) General Description System Advisor Model. Tech. Rep. NREL/TP-6A20-70414; 2018.

[64] Bejan A, Tsatsaronis G, Moran M. Thermal Design & Optimization. Wiley; 1996.

[65] Fleming DD et al., Scaling Considerations for a Multi-Megawatt Class Supercritical CO2 Brayton Cycle and Commercialization, SANDIA REPORT SAND2013-9106; 2013.

[66] https://www.matche.com/equipcost/Exchanger.html.

[67] Driscoll MJ, Hejzlar P. 300 MWe Supercritical CO2 Plant Layout and Design. MIT Nuclear Engineering Department (2004), MIT-GFR-014.

[68] Purohit GP. Estimating costs of shell-and-tube heat exchangers. Chem Eng 1983;22:56–67.

[69] Vatavuk WM. Updating the CE Plant Cost index. Chem Eng 2002;109:62–70.

[70] Wagner MJ. SolarPILOT. Software version 1.3.8. Golden, Colorado, USA: National Renewable Energy Laboratory (NREL); 2018. https://www.nrel.gov/csp/solarpilot.html.